Materials Advances

ROYAL SOCIETY OF CHEMISTRY

PAPER

View Article Online
View Journal | View Issue

Open Access Article. Published on 06 January 2026. Downloaded on 3/22/2026 11:27:01 AM.
This article is licensed under a Creative Commons Attribution-NonCommercial 3.0 Unported Licence.

Check for updates

Cite this: *Mater. Adv.*, 2026, 7, 2159

Mechanistic insights into graphene oxide-enhanced single electrospun PMMA fibres achieved *via* surface interface engineering

Anushree S. Bhat, †[a] Jonaid Ahmad Malik, †[b] Madhusudhana M. Devadiga,[a] Irfan Ayoub,[c] Ganesh Chandra Nayak,[d] Nannan Wang,[e] Javed N. Agrewala*[b] and Santosh K. Tiwari *[a]

Received 2nd September 2025,
Accepted 3rd January 2026

DOI: 10.1039/d5ma01000d

rsc.li/materials-advances

Herein, we focus on optimising the electrospinning parameters to fabricate well-defined, physically distinct cotton-like fibres of polymethyl methacrylate (PMMA) with the incorporation of 0.39 wt% graphene oxide (GO). So-fabricated cotton-like distinct single fibres were extensively characterised by employing advanced techniques like high-resolution transmission electron microscopy (HRTEM) to study the internal structure and atomic force microscopy (AFM) to evaluate the mechanical properties of the single fibres at the nanoscale to overcome the ambiguities associated with the conventional mechanical property testing for a fibrous mat. The studies revealed that the fibres produced were highly flexible (DMT modulus ∼ 0.28 GPa) with exceptional thermo-mechanical performances and cryogenic stability. Also, the probable underlying mechanism and the molecular-level interaction of PMMA–GO have been discussed thoroughly. The biocompatibility of PMMA–GO single fibres has been examined by the cell viability test. The findings demonstrated that PMMA–GO fibres are non-toxic to cells at higher GO concentrations. Importantly, this study is directed towards the comprehensive characterisation of single electrospun fibres, thereby investigating their behaviour in a cryogenic (liquid nitrogen) environment.

1 Introduction

Meeting the demands of next-generation technologies requires materials that combine functionality, adaptability, and resilience under extreme conditions.[1] Among these, polymeric nanofibres have emerged as highly versatile candidates, offering increased surface area, tailorable porosity, and exceptional mechanical flexibility. These features permit applications in filtration, sensing, energy storage, tissue engineering, and smart textiles.[2] The ability of such fibres to integrate nanoscale functional materials can impart tailored conductivity, selective permeability and stimuli-response behaviour, making them indispensable in fields like aerospace,[3] electronics, and biomedicine.[4,5] Most of the acrylate thermoplastics exhibit severe embrittlement, loss of ductility, and reduced impact resistance at temperatures between −20 °C and 60 °C,[6] limiting their utility in demanding environments. These shortcomings are primarily evident in amorphous thermoplastics like PMMA, despite their physicochemical adaptability and widespread use. Consequently, their vulnerability to brittle failure and low thermal stability, $T_g \cong 100$ °C,[7] can restrict their suitability for use under extreme conditions, especially in aerospace and defence applications.

To address these constraints, fibre-level engineering through electrospinning offers a transformative strategy. Electrospinning is a flexible and scalable method for the fabrication of polymeric mats with ultrafine fibres ranging from the microscale to the nanoscale. However, the fabrication of single distinct polymeric fibres, by electrospinning as opposed to mats[8] and bundles, requires precise control of parameters, including solution properties, flow rate and ambient conditions. Understanding these parameters is crucial for fabricating fibres that can survive extreme environmental conditions. Notably, recent studies have demonstrated the feasibility of forming unconventional three-dimensional (3D) fibrous macrostructures, largely cotton-wool-like morphologies, through controlled electrospinning conditions.[9] Schneider *et al.*[9] reported cotton-like poly(lactide-*co*-glycolide) nanocomposites with promising

[a] *Centre for New Materials and Surface Engineering, Department of Chemistry, NMAM Institute of Technology (NMAMIT), Nitte (Deemed to be University), Nitte 574110, Karnataka, India. E-mail: ismgraphene@gmail.com*
[b] *Immunology Laboratory, Department of Biomedical Engineering, Indian Institute of Technology Ropar, Rupnagar, 140001, India. E-mail: jagrewala@gmail.com*
[c] *Department of Metallurgical Engineering and Materials Science, Indian Institute of Technology Bombay, Mumbai, 400076, India*
[d] *Department of Chemistry and Chemical Biology, IIT (ISM), Dhanbad, Jharkhand, 826004, India*
[e] *State Key Laboratory of Featured Metal Materials and Life-cycle Safety for Composite Structures, School of Resources, Environment and Materials, Guangxi University, Nanning, Guangxi 530004, China*
† These authors contributed equally.

© 2026 The Author(s). Published by the Royal Society of Chemistry

Open Access Article. Published on 06 January 2026. Downloaded on 3/22/2026 11:27:01 AM. This article is licensed under a Creative Commons Attribution-NonCommercial 3.0 Unported Licence.

in vitro bioactivity, whereas Zhou *et al.*[10] fabricated comparable structures using centrifugal melt-spinning of poly(lactic acid) (PLA) for tissue engineering applications. Derivatives of PLA have been extensively studied for producing 3D scaffolds with hierarchical nano-/microfibre structures, including core–shell architectures designed for regenerative medicine. Although progress has been made, the mechanistic basis of cotton-wool-like morphology formation remains an open question.[9] Indeed, findings suggest that polymer–solvent interactions and spontaneous self-assembly may contribute significantly to the development of such structures.[9]

Unlike bulk films and non-woven mats, single electrospun fibres present a novel combination of material properties and structural features that are highly desirable for advanced applications. In such morphologies, the individual fibres are visually distinct and physically isolated, enabling direct, accurate measurement of thermomechanical properties, controlled investigation of fibre morphology, alignment, and defect structures, as well as controlled surface functionalisation at the single fibre level.[11] Although studies have explored the electrospinning of PMMA and its composites to fabricate membranous mats for applications in water filtration,[12] optics, and biomedical scaffolds,[13] clear investigations into their performance under cryogenic conditions, particularly at the single fibre scale, remain minimal. Chen *et al.* reviewed the performance and modification strategies of polymers for cryogenic applications, emphasising methods to improve their mechanical properties and compatibility with extremely low temperature environments, such as the incorporation of nanomaterials and tailored polymer networks.[14] Nanofiller reinforcements, especially with GO, can substantially increase the thermomechanical performance of polymer fibres.[15] GO offers exceptional mechanical strength, thermal stability and interfacial adhesion with polymer matrices. Qu *et al.* demonstrated that incorporating GO into epoxy resin significantly enhances the cryogenic mechanical properties of carbon fibre reinforced composites, with optimal performance at 77 K achieved at 0.2 wt% GO due to improved interfacial adhesion and matrix reinforcement.[16] However, its role in modifying the endurance property of electrospun polymer fibres under low-temperature cryogenic conditions has not been systematically addressed.

As far as we are aware, we report the first fabrication of cotton-wool-like fibrous (single fiber) materials based on PMMA using a tetrahydrofuran (THF) solution system, further integrated with synthesised GO-nanosheets. The resulting low dimensional fibrous structures, derived from both neat and GO-reinforced PMMA, reflect a distinct morphology markedly different from conventional cotton-wool-like materials. Comprehensive morphological, physicochemical, and thermo-mechanical analyses were conducted to assess structural fidelity and functional performance. A special focus was given to the evaluation of the mechanical properties of individual fibres using AFM, which offers distinct advantages over conventional methods like micro-tensile testing, typically carried out for bulk fibrous mats. The probable mechanism of cotton-wool-like fibrous system formation has also been proposed (Tiwari hypothesis). Strikingly, these engineered structures retain mechanical flexibility and structural integrity at sub-zero, cryogenic temperatures, indicating promising applications in extreme environments.

2 Experimental section

2.1 Materials and methods

PMMA with a molecular weight of ~330 000 g mol^{-1} was obtained from LG2-S, Sumitomo Chemical Company Ltd. Natural graphite (99.8% purity) was obtained from Sigma Aldrich, Bangalore, India. High purity solvents and reagents - THF (≥99.9%), phosphoric acid (H_3PO_4) (85%), and sulphuric acid (H_2SO_4) (≥98%), were acquired from Spectrum Reagents and Chemicals Pvt. Ltd, India. Potassium permanganate ($KMnO_4$) was brought from Merck Life Science Pvt. Ltd, India. Hydrogen peroxide (H_2O_2) was sourced from Thermo-Fischer Scientific India Pvt. Ltd, India. Deionised water was available in the laboratory. All the chemicals used were as-received without any further purifications. A coaxial electrospinning set-up, with high voltage 0–30 kV, with a programmable syringe pump, was acquired from Pico Chennai, India. All the instruments, like the weighing balance, magnetic stirrer, probe sonicator, centrifuge machine, and vacuum oven, required for the experiment were accessible in the laboratory.

2.2 Synthesis of GO

GO was synthesised *via* a modified Hummer's method[17] using 200 mL of a 9 : 1 mixture of concentrated H_2SO_4 and H_3PO_4 to oxidize 1.5 g of natural graphite. The mixture of acids was slowly added to ensure controlled intercalation, followed by gradual addition of 9 g of $KMnO_4$ at 50 °C to mitigate uncontrolled exothermic reaction during the process of oxidation. The reaction temperature was then raised to 65 °C with continuous stirring for 16 hours to achieve complete oxidation while maintaining structural integrity through the buffering effect of the mixture of acids. The oxidation process was terminated by quenching with 200 mL of ice and 1.4 mL 30% H_2O_2 to reduce residual oxidants. Subsequent purification was done through centrifugation and sequential washings with deionised water, H_2O_2, and ethanol to remove acidic and metallic impurities. The purified GO was dried at 80 °C overnight, yielding a black powder with characteristic oxygen functionalities, which are confirmed by spectroscopic analysis. Fig. 1 demonstrates the schematic for the synthesis of GO. For the detailed characterisation of GO, refer to Sections 2.1 and 2.2 and Fig. P1, SI.

2.3 Electrospinning of PMMA fibres

During the experiment, the electrospinning process involved dissolving 1.5 g of PMMA granules in 32 mL of THF, followed by 3 hours of vigorous stirring and overnight equilibration to enable complete polymer dissolution and optimal chain entanglement. The homogenous solution was loaded into a syringe fitted with a metallic needle, having an inner bore of 1.0 mm of needle, and subjected to electrospinning at a voltage of 15 kV with a precisely controlled feeding rate of 0.15 mL min^{-1}. An aluminium foil-covered grounded collector, translating at a speed of 500 mm h^{-1}, was positioned 12 cm away from the needle tip to

 © 2026 The Author(s). Published by the Royal Society of Chemistry

Open Access Article. Published on 06 January 2026. Downloaded on 3/22/2026 11:27:01 AM.
This article is licensed under a Creative Commons Attribution-NonCommercial 3.0 Unported Licence.

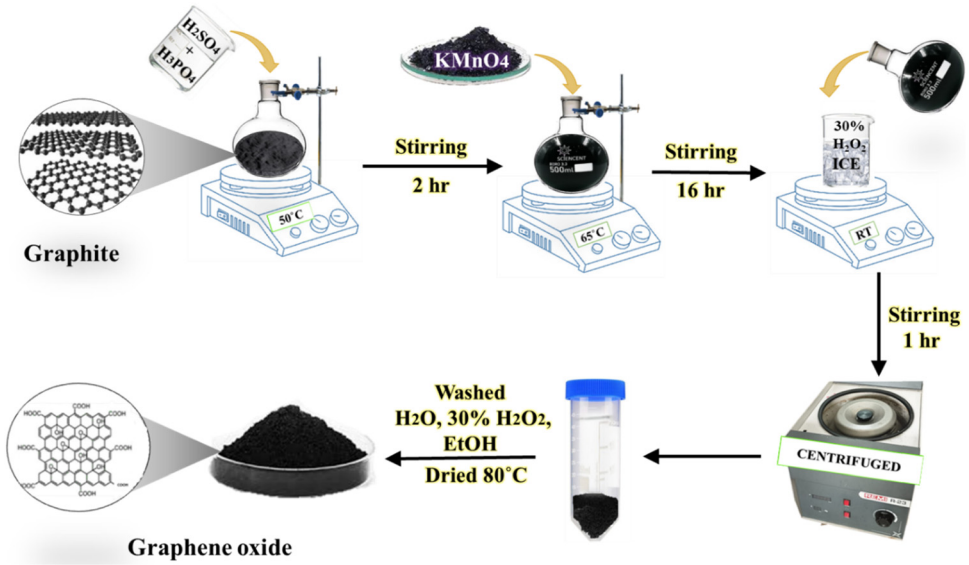

Fig. 1 Synthesis of GO from its precursor, graphite. The steps involve oxidation in the presence of a mixture of acids and $KMnO_4$, followed by quenching, repeated washing, and drying to obtain GO, as the final product.

collect the fibres. The temperature and the relative humidity were 23 °C and 65%, respectively. The moderately high humidity could also have contributed to the formation of pores in the fabricated fibres and is consistent with THF-based electrospinning.[18] Upon application of high voltage, electrostatic forces overcame surface tension to form a Taylor cone that ejected a charged jet. The jet underwent bending instabilities, induced by the charge repulsion and viscoelastic forces, leading to significant jet thinning, resulting in deposition of ultrafine, cotton-like PMMA fibres. The rapid evaporation of THF guaranteed solidification of the fibres into a non-woven mat with submicron-scale fibre diameters. The fibres were collected on a metallic grounded collector. To obtain individually distinct fibres without disturbing their morphology, a metallic grid was also used for collection (as shown in Fig. 9i a).

2.4 Electrospinning of PMMA–GO composite fibres

6 mg (= 0.39 wt%) of GO was first dispersed in 30 mL of THF using a probe sonicator. Sonication was performed at 70% amplitude (estimated delivered power – 455 W), with a pulse cycle of 3 s ON/1 s OFF for 15 minutes by maintaining a probe temperature of 25–30 °C to minimise solvent evaporation and ensure uniform dispersion. To the resulting homogenously dispersed solution, 1.5 g of PMMA was added and stirred for 3 hours at 40 °C, followed by sonication to achieve complete dissolution and homogenisation. The solution was kept aside for 24 hours at 25 °C to achieve extensive solvation and solvent evaporation. The obtained solution was electrospun as mentioned above. Information about the code and composition of different samples is provided in Table 1. Also, the schematics of all the steps involved in the overall synthesis process are well presented in Fig. 2.

2.5 Characterisation

Advanced electron microscopic techniques were employed to analyse the surface morphology, utilising a Hitachi S-4800 field emission scanning electron microscope (FESEM), Japan. HRTEM analysis was performed using high-angle annular dark-field scanning transmission electron microscopy (HAADF-STEM) functionality at an accelerating voltage of 80–100 eV. Electrospun fibres were placed on the carbon-coated copper grids. Lattice fringes and interfacial characteristics were analysed. Selected area electron diffraction (SAED) patterns were used to verify crystallinity. Elemental composition was verified by energy-dispersive X-ray spectroscopy (EDS). Powder X-ray diffraction (XRD) analysis was carried out using a Rigaku D/MAX 2500 V diffractometer (Japan) equipped with Cu Kα radiation (λ = 0.15498 nm), operating at 40 kV and 100 mA. The diffraction patterns were recorded over a 2θ range of 5°–80° at a scanning speed of 5° min^{-1} to investigate the crystallite structure. Chemical functionality was characterised using a PerkinElmer Spectrum 100 Fourier-transform infrared (FTIR) spectrometer, with spectral acquisition from 400 to 4000 cm^{-1}. Nanoindentation AFM measurement of fabricated fibres was performed with a Nanoscope AFM instrument, Bruker, Germany. By recording force–distance curves, the local elastic modulus was extracted. An X-ray photoelectron spectroscopy (XPS)-PHI Quantera II system with a monochromatic Al Kα radiation source was employed to investigate the elemental composition and chemical bonding states.[19] The spectra were recorded with a pass energy of 20 eV and an energy step size of 0.1 eV. Charge neutralisation was applied during the measurements to

Table 1 Sample codes and adopted preparation/synthesis methods, along with their composition

Sl. no.	Sample code	Composition
1.	S1 (neat granules)	Pure PMMA
2.	S2 (solution casting film)	Pure PMMA + GO
3.	S3 (electrospun fibre)	Pure PMMA
4.	S4 (electrospun fibre)	Pure PMMA + GO

Open Access Article. Published on 06 January 2026. Downloaded on 3/22/2026 11:27:01 AM.
This article is licensed under a Creative Commons Attribution-NonCommercial 3.0 Unported Licence.

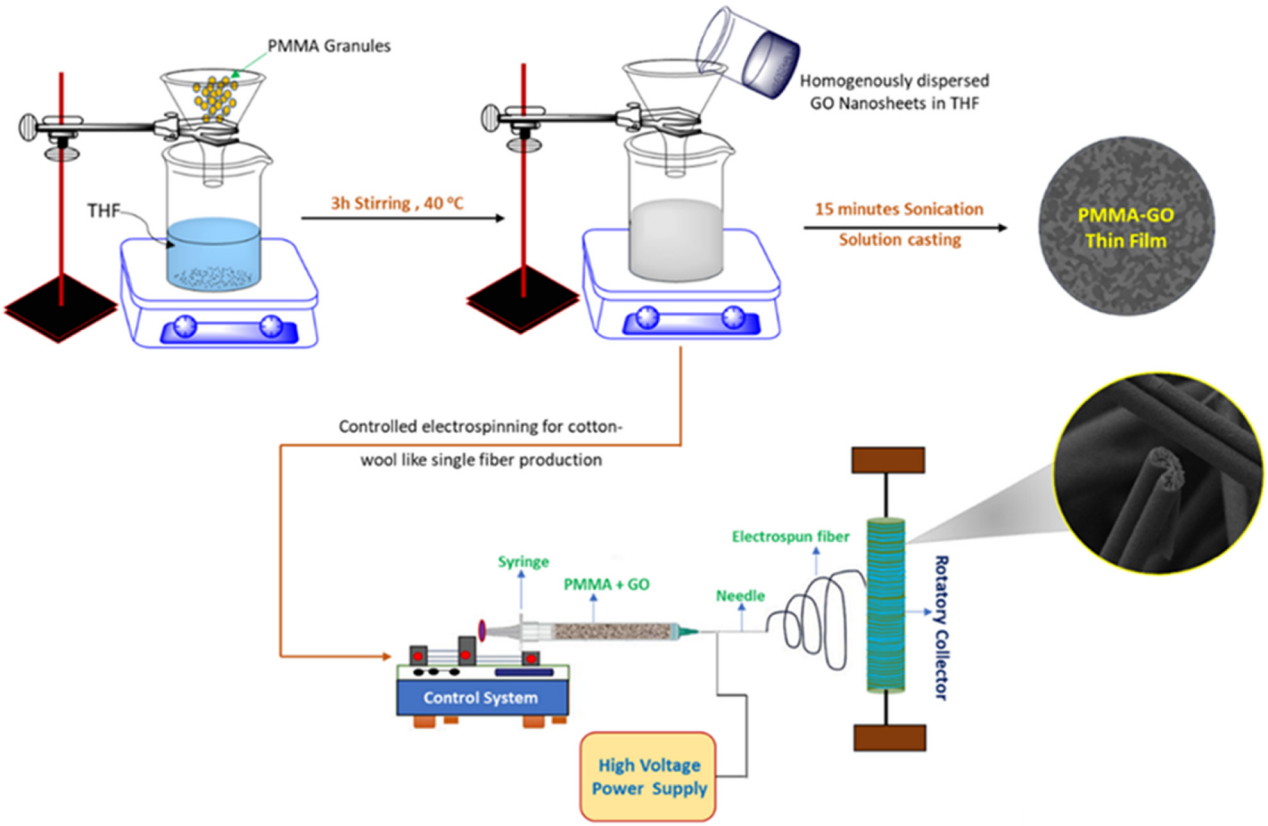

Fig. 2 Schematic representation depicting all the steps involved in fabricating the physically distinct cotton-like GO reinforced PMMA fibres by electrospinning. Initially, the GO was dispersed homogenously in THF followed by the addition of PMMA granules and stirring the solution for 3 hours at 40 °C. Subsequently, the solution was electrospun to fabricate fibres by carefully optimising electrospinning parameters.

compensate for surface charging effects. Thermogravimetric analysis (TGA) was employed to assess the thermal properties. The sample was heated from 30 °C to 770 °C with a heating rate of 5 °C min^{-1}, under a N_2 atmosphere.

3 Results and discussion

3.1 Microscopic analysis

3.1.1 FESEM analysis. The FESEM image of pure bulk PMMA granule S1 (Fig. 3ii, S1) shows a smooth and homogeneous surface, authenticating the uniformity of the polymer matrix. No phase separation or heterogeneous inclusions were observed, consistent with the characteristic morphology of bulk PMMA as previously reported.[20] In contrast, the FESEM micrographs (Fig. 3ii, S2) of S2 show slightly roughened surfaces with numerous tiny pores throughout, which is due to the incorporation of GO sheets and the extrusion of gases during drying.[21] In most regions, the GO nanosheets appear to be well-dispersed, as no large agglomerates are detected, and the film maintains structural continuity. The observed increase in surface roughness supports the successful integration of GO and suggests potential interfacial interactions, as well as the formation of pores and cracks (inset, Fig. 3ii, S2) caused by gas removal during solvent evaporation. Electrospun pure PMMA nanofibres, S3 (Fig. 3ii), are characterised by randomly oriented, continuous fibres. The FESEM images show smooth fibre surfaces, uniform diameters, and interconnected porous networks, S3 (inset, Fig. 3ii). The absence of bead formation indicates that electrospinning conditions were optimised. Furthermore, the lack of prominent surface features reflects the amorphous nature of PMMA. Although the fibres in the pure electrospun PMMA are interconnected, they are not highly branched. Similarly, the FESEM images of PMMA–GO nanofibres, S4 (Fig. 3ii), unveil a comparable cotton-wool-like architecture with randomly distributed fibres. However, the individual fibres are more distinct and often have branching. Careful examination identifies a high degree of porosity in PMMA–GO electrospun fibres. The porous structure enhances surface area, reducing thermal conductivity for better insulation and accommodating strain to improve cryogenic durability. Overall, the morphology remains highly porous and fibrous, and the incorporation of GO nanosheets contributes to increased fibre compactness and straightness, with branching features corroborated by HRTEM analysis. EDS analysis was employed to verify the elemental composition and spatial distribution of GO within the PMMA matrix, confirming the uniform dispersion of GO (refer to Section 2.5, Fig. P3, SI).

3.1.2 TEM analysis. Both TEM and HRTEM images of neat PMMA single nanofibres are presented (Fig. 3iii), providing detailed insight into the surface and internal microstructure at

 © 2026 The Author(s). Published by the Royal Society of Chemistry

Open Access Article. Published on 06 January 2026. Downloaded on 3/22/2026 11:27:01 AM.
This article is licensed under a Creative Commons Attribution-NonCommercial 3.0 Unported Licence.

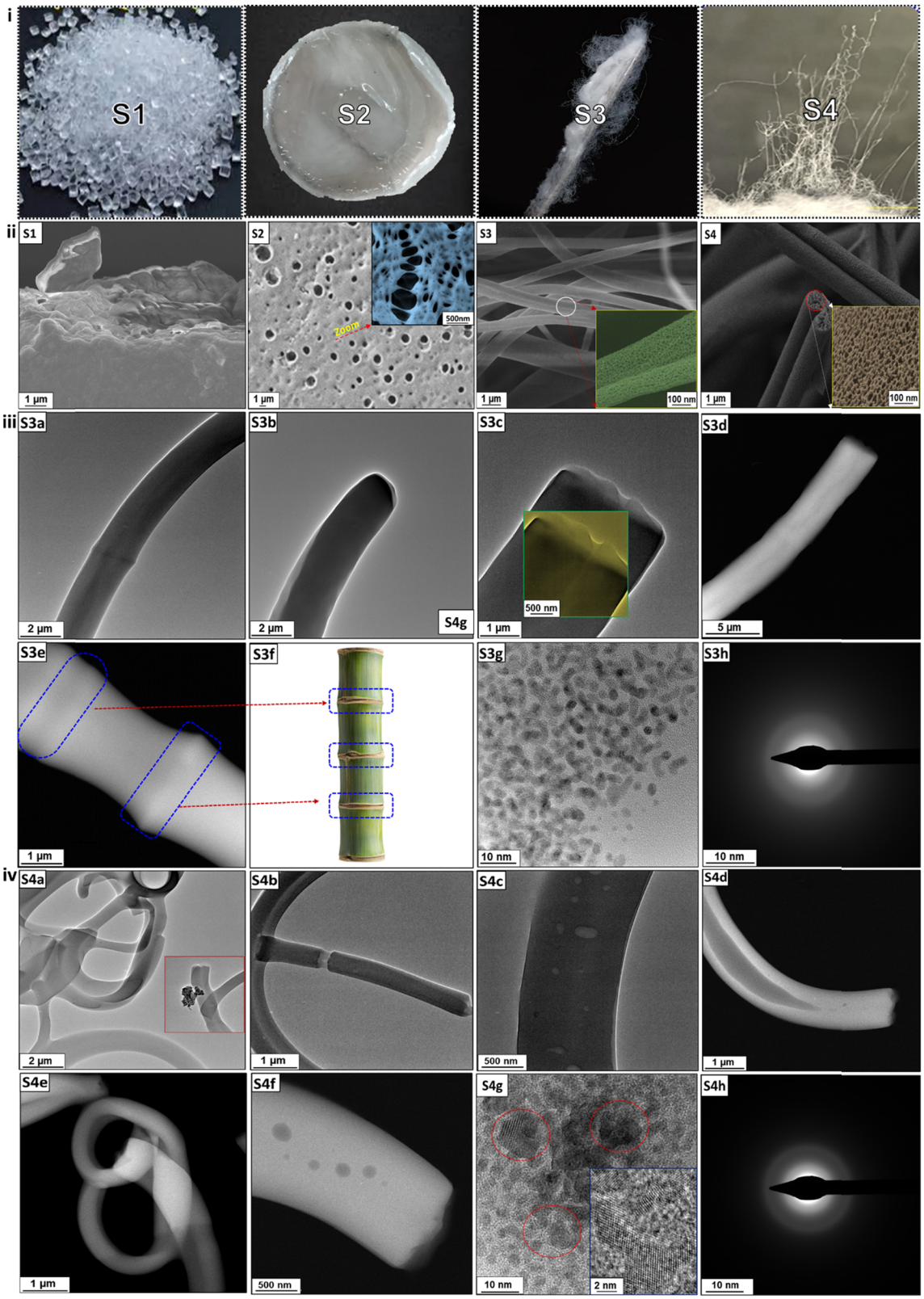

Fig. 3 (i) S1 - neat PMMA granules, S2 - solution casting for PMMA–GO, S3 - electrospun fibres of neat PMMA, S4 - electrospun fibres of PMMA–GO. (ii) FESEM images of S1–S4 samples. The inset shows a magnified view of selected regions of S2, S3 and S4, highlighting morphological details at varying scales. (iii) TEM, HRTEM and SAED analyses of neat PMMA electrospun fibres. S3a–S3c: TEM images of neat PMMA depicting uniform and smooth neat PMMA fibres. The S3c image confirms the amorphous structure. S3d and S3e illustrate dark field TEM images showing consistent fibre morphology. S3f: the bamboo image serves as a visual reference, emphasising the continuous, nodal, and internodal architecture of PMMA fibres. S3g: the HRTEM image showing the amorphous structure. S3h: the SAED pattern showing a diffuse halo, affirming the amorphous nature. (iv) The TEM image of PMMA–GO nanofibres, the inset in S4a showing regions of GO aggregation. S4b: the TEM image showing regions of origin of bifurcation. S4c: the higher magnification TEM image showing GO dispersed regions. S4d–S4f: dark-field TEM images, with darker regions showing dispersion of GO within the PMMA matrix. S4g: the HRTEM image showing amorphous PMMA with embedded GO (circled regions and the inset shows lattice fringes). S4h: the SAED pattern showing a halo superimposed faintly, indicating the presence of crystalline GO within the amorphous PMMA matrix.

Open Access Article. Published on 06 January 2026. Downloaded on 3/22/2026 11:27:01 AM.
This article is licensed under a Creative Commons Attribution-NonCommercial 3.0 Unported Licence.

the nanoscale. TEM and HRTEM analyses consistently reveal an amorphous morphology throughout the nanofibre matrix for S3. The TEM images (Fig. 3iii, S3a–S3c) illustrate a slightly blended texture and a supernodal ridge structure resembling that of bamboo (Fig. 3iii, S3f), with no observable crystalline domains and lattice fringes. This affirms the entirely non-crystalline nature of PMMA, which is consistent with its atactic polymer configuration that prevents ordered chain packing.[22] The edges of the fibres are smooth and diffuse, showing no signs of structural discontinuities. However, the presence of a supernodal ridge and sharp phase boundaries in the HRTEM image (Fig. 3iii, S3e) is identified as a unique morphological feature. This may be attributed to localised densification or chain entanglements induced during the fibre formation process, potentially due to rapid solvent evaporation and electrostatic stretching effects during electrospinning. Upon careful observation of images (Fig. 3iii, S3c and S3d), significant contrast variations can be discerned, likely arising from local differences in fibre thickness. Additionally, the TEM images confirm that the nanofibres are solid and not hollow, as observed in Fig. 3iii, S3c.[23]

PMMA–GO nanofibres, unveiling a unique cotton-wool-like morphology, exhibit distinct microstructural differences in both TEM and HRTEM images. The incorporation of GO nanosheets introduces regions of enhanced contrast and increased structural heterogeneity (Fig. 3iv, S4a–S4f). Within the amorphous PMMA matrix, embedded GO nanosheets are identified by their wrinkled morphology and high-contrast appearance, indicative of their electron-dense nature. These sheets are often aligned along the fibre axis, although some appear randomly oriented within the matrix. In well-dispersed systems, GO is observed as few-layer sheets with low transparency due to the surrounding PMMA fibres and their wavy texture. Although dispersion is generally uniform, minor aggregation can be observed (inset, Fig. 3iv, S4a). The interaction between PMMA and GO results in close interfacial contact, often conveying a gradual transition zone where the polymer appears to interpenetrate the GO layers (Fig. 3iv, S4c and S4f). This suggests strong interfacial adhesion, likely facilitated by hydrogen-bonding (H-bonding) between PMMA's –C═O groups and GO's oxygen-containing functional groups (Fig. 11). In regions where GO retains partial graphitic order, lattice fringes with a *d*-spacing of ~0.65 nm have been reported, matching the (001) interlayer spacing of GO.[24] The visibility of these fringes depends on the degree of dispersion and the orientation of the nanosheets relative to the electron beam. In the present study, the absence of very visible lattice fringes in most regions validates a high degree of dispersion and effective dispersion of GO within the PMMA matrix. Conversely, in less uniform areas, overlapping GO sheets can appear as darker, multilayer regions with more prominent lattice fringes, indicating incomplete exfoliation.[25]

Notably, unlike pure PMMA nanofibres, the PMMA–GO nanofibres highlight significant branching and morphological complexity. This enhanced branching (Fig. 3iv, S4a, S4b, and S4e) is likely due to the presence of GO, which can locally modify the electrospinning jet dynamics through changes in solution conductivity, viscosity, and surface charge density.[26] GO nanosheets having polar functional groups may also influence fibre solidification and phase separation during electrospinning, resulting in a more branched network architecture.[27] This is due to disruption in polymer chain alignment and electrospinning dynamics. During fibre formation, PMMA chains adsorb on GO sheets *via* various bonding and non-bonding interactions (Fig. 11 and 12), reducing bulk entanglement and creating asymmetric stress zones that promote bifurcation of the fibres. The rigid structure of GO further perturbs the jet, triggering secondary branching due to localised charge variations or viscoelastic instability. The branching point can act as a crack deflector, dispersing the mechanical stress under cryogenic conditions, preventing brittle fracture. These structural features directly correlate with the enhanced functional properties observed in PMMA–GO nanocomposites, including amplified mechanical strength, thermal stability, and potential applications in barrier and sensing technologies.

3.1.3 STEM and SAED analyses. To accurately investigate the impact of GO nanosheet incorporation on the crystallinity and structure of PMMA fibres, STEM and SAED analyses were performed. The STEM images (Fig. 3iii, S3g) of pure PMMA nanofibres show smooth, homogeneous, and amorphous structures, uniform contrast, and relatively featureless interiors, consistent with the polymer's inherently non-crystalline nature.[28] The fibres depict a slightly flattened morphology with minimal internal texture. The conforming SAED patterns (Fig. 3iii, S3h) show diffuse halos, characteristic of amorphous polymers, indicating the absence of long-range crystalline order, as previously reported.[29] These diffuse rings arise from the disordered arrangement of PMMA chains and the lack of any periodic lattice planes and are further discussed in the XRD analysis section. Upon incorporation of GO nanosheets into the PMMA matrix, the STEM images (Fig. 3iv, S4g) reveal increased internal contrast, manifested as dark, wrinkled, flake-like domains embedded within the polymer matrix. These domains correspond to GO sheets, which are denser and more electron-rich than PMMA. The GO sheets are often aligned along the fibre axis, facilitated by optimised electrospinning parameters and high-quality dispersion. The overall morphology becomes highly heterogeneous, with interconnected features induced by GO-mediated modulation of electrospinning dynamics. The SAED patterns of PMMA–GO nanofibres show a combination of amorphous halos from PMMA and weak, discrete diffraction spots, resembling arcs typically associated with partially ordered GO sheets (Fig. 3iv, S4h). Due to the high degree of dispersion, the sharp crystalline signals of GO are mostly absent, indicating effective dispersion. Nevertheless, localised multilayer regions may still produce (001) diffractions, corresponding to interlayer spacings of approximately 0.65 nm. The appearance of these features in the SAED patterns signifies structural heterogeneity and enhanced interfacial organisation, which correlate with the improved mechanical, thermal, and functional properties of the PMMA–GO composite fibres.

3.2 Spectroscopic analysis

3.2.1 XRD analysis. The XRD pattern of neat PMMA granules validates a broad amorphous halo centred around

 © 2026 The Author(s). Published by the Royal Society of Chemistry

Open Access Article. Published on 06 January 2026. Downloaded on 3/22/2026 11:27:01 AM.
This article is licensed under a Creative Commons Attribution-NonCommercial 3.0 Unported Licence.

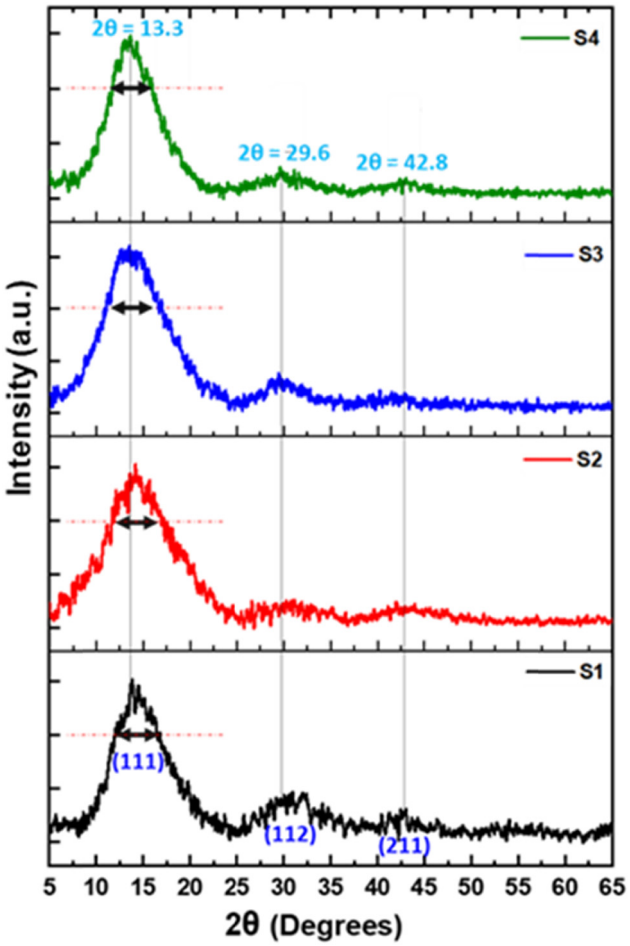

Fig. 4 XRD spectrum of S1–S4, showing the effect of GO nanosheets at the interfaces of PMMA. It represents the broad amorphous halo peaks ~13.3° for PMMA–GO fibres, consistent with the PMMA–GO cast film and neat PMMA fibre.

$2\theta \approx 13.3°$, which corresponds to the (111) reflection, S1 (Fig. 4). This broad scattering is characteristic of the amorphous nature of PMMA, as well established in the literature.[30] The diffuse halo arises from short-range ordering between the polymer chains and indicates the absence of long-range periodicity due to disordered chain packing. The atactic molecular configuration of PMMA, characterised by a random stereochemistry along the polymer backbone, hinders the formation of crystalline domains, reinforcing its intrinsically amorphous nature. Consequently, sharp Bragg reflections typically associated with crystalline materials are absent in the XRD spectrum. In addition to the main amorphous halo, very weak and broad peaks are observed at around $2\theta \approx 29.6°$ (112) and $2\theta \approx 42.8°$ (211), which have been reported for PMMA and its nanocomposites.[31] These features may be attributed to weak interchain correlations and residual order but are not indicative of true crystallinity. The XRD pattern of cotton-wool-like electrospun PMMA nanofibres also presents a broad amorphous halo centred around $2\theta \approx 13.3°$ (111), consistent with the amorphous nature of PMMA for S3 (Fig. 4). Despite the high shear and elongational forces imparted during the electrospinning process, which can, in some polymers, induce molecular alignment and partial crystallinity, PMMA remains amorphous. This is due to the rigidity of its backbone and its atactic configuration, which limit the extent of any induced order. Interestingly, the amorphous halo nanofibres appear slightly broader than those in bulk PMMA. This broadening is attributed to differences in chain packing density, nanoscale fibre morphology, and rapid solvent evaporation during fibre formation, all of which can influence the local chain environment and short-range ordering for S3 (Fig. 4).

The XRD pattern of PMMA–GO nanocomposite films, prepared *via* solution casting (Fig. 4), retains the broad amorphous peak of PMMA at $2\theta \approx 13.3°$ (111).[32] Notably, the characteristic diffraction peak of GO near $2\theta \approx 10°$, corresponding to the (001) reflection, is entirely merged with the PMMA halo for S3 (Fig. 4). In the electrospun PMMA–GO nanofibres, S4 (Fig. 4), the XRD pattern reflects features consistent with both pure PMMA fibres and the PMMA–GO cast films. However, the GO (001) peak is highly broadened, further supporting the hypothesis of effective exfoliation and nanoscale dispersion. The pattern with a *d*-spacing of 0.65 nm, as calculated from Bragg's equation, signifies the wrapping of PMMA chains between GO sheets. This substantiates the strong PMMA–GO interfacial interactions, disrupting the lamellar stacking of GO. The broadened peak further evidences a high degree of GO exfoliation and uniform dispersion within the PMMA matrix, critical for enhancing cryogenic stress dissipation. The high shear forces and rapid elongation during electrospinning contribute to the delamination and uniform distribution of GO nanosheets. Moreover, the disappearance of distinct GO peaks for the nanofibre composite suggests strong interfacial interactions and homogeneous integration of GO within the amorphous PMMA matrix. This is indicative of a well-dispersed nanocomposite architecture, where GO nanosheets are either embedded within or coated over the PMMA fibres (Fig. 12), enhancing structural compatibility and potentially improving functional properties. The functional moieties in the studied samples are briefed in the FTIR analysis section.

3.2.2 FTIR analysis. FTIR spectral data for the samples S1–S4 are given in Fig. 5. A strong band near ~1727 cm^{-1} is attributed to the stretching vibration –C═O of the ester group of PMMA chains; prominent bands in the range of ~1140 cm^{-1} are owing to –C–O asymmetric stretching, whereas the band at ~1238 cm^{-1} is attributed to symmetric vibrations of the –C–O linkage from PMMA, with potential contributions from the –C–O–C– group of GO. Other peaks observed at ~2950 cm^{-1} represent $-CH_2$ and $-CH_3$ stretching. The peak at ~1434 cm^{-1} corresponds to –C–H asymmetric bending vibrations of the methyl ($-CH_3$) group of PMMA and C–H symmetric bending vibrations of the $-CH_3$ groups of the PMMA side chain observed at ~1385cm^{-1}. The bands at ~985 cm^{-1} and ~750 cm^{-1} are derived from $-CH_2$ wagging and rocking modes, respectively. These spectral features reflect the ester functionalities and aliphatic backbone of atactic pure PMMA. Remarkably, although S2 and S4 exhibit all the characteristic peaks of their bulk counterpart, they also exhibit an additional peak at ~2363 cm^{-1} (Fig. 5), which may be due to the adsorption of atmospheric carbon dioxide (CO_2).[33] Owing to the presence of oxygen-rich functionalities and

Open Access Article. Published on 06 January 2026. Downloaded on 3/22/2026 11:27:01 AM.
This article is licensed under a Creative Commons Attribution-NonCommercial 3.0 Unported Licence.

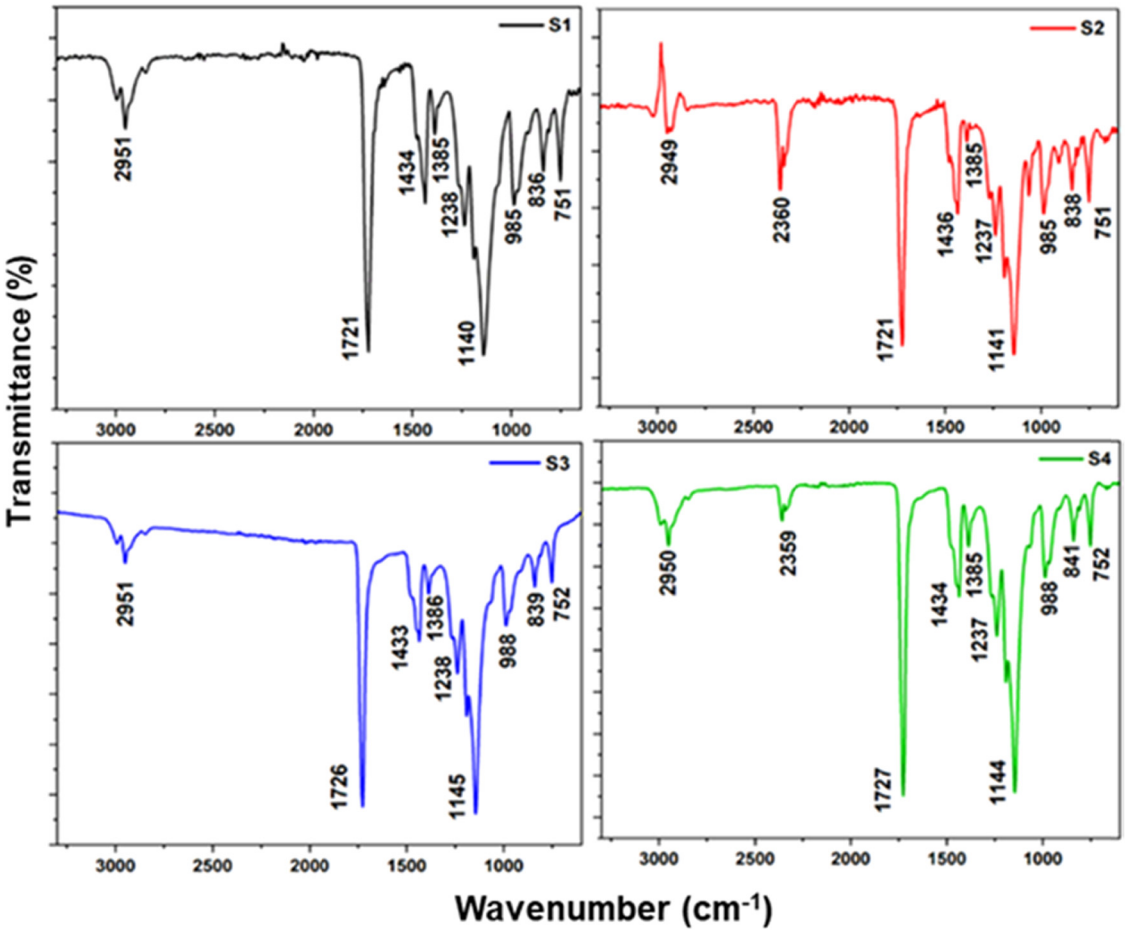

Fig. 5 FTIR spectra are consistent with the different fabricated samples S1–S4. The spectra show a subtle shift in the peaks for S4, suggesting considerable interfacial interaction between PMMA chains and GO sheets.

high surface area, GO can readily adsorb ambient CO_2;[34] also, –C═O in PMMA has the affinity for CO_2.[35] S2 with denser aggregation of GO provides more sites for CO_2 adsorption, resulting in a high-intensity peak as compared to S4. In the PMMA–GO film prepared by solution casting, the FTIR spectrum retains all characteristic PMMA peaks but conveys noteworthy shifts and broadening, particularly in the –C═O region. There is a subtle shift in the position and intensity of the –C═O peak for S3 and S4, indicating changes in the local environment of –C═O due to differences in molecular packing and slight changes in crystallinity induced by the electrospinning process. Electrospinning involves stretching and orienting the chains along the fibre axis due to the electric field and rapid solvent evaporation. The slight increase in the intensity of the –C=O peak in S4 can be attributed to the morphological difference between bulk and fibrous structure. In the bulk (granular) form, most of the –C=O groups are buried within the polymeric matrix, making them less accessible to interact with the IR beam, whereas in the fibrous structure, the significantly larger surface area enhances the exposure of these functional groups. The increased intensity of S4 as compared to other samples likely results from GO integration, which enhances the exposure of –C═O of PMMA chains during electrospinning. This promotes –C═O accessibility within the high surface area fibres, potentially boosting the IR activity, due to changes in local packing of PMMA chains.[32] Also, direct identification of GO peaks in S2 and S4 is challenging due to the very small quantity of GO in the PMMA matrix. However, the slight shifts observed suggest changes in the chemical environment of the PMMA functional group due to GO incorporation. The characteristic FTIR features for S4 are summarised in Section 2.4, Table P1, SI.

3.2.3 XPS analysis. From FTIR analysis, we observed the interaction of GO nanosheets with PMMA functional moieties. Herein, the XPS spectrum of PMMA–GO nanofibres very clearly reveals the successful incorporation of GO into the polymer matrix and elucidates the chemical states of elements involved, primarily carbon and oxygen, at the fibre surface. The survey spectrum (Fig. 6, S4a) of the PMMA–GO nanofibres demonstrates dominant peaks for C 1s and O 1s, which represent carbon and oxygen, the major constituents of both PMMA and GO. Compared to pure PMMA nanofibres, which exhibit a relatively high C/O atomic ratio due to the predominance of hydrocarbon and ester functionalities,[36] the presence of GO introduces additional oxygen-containing groups such as hydroxyl (–OH), epoxide, –C═O, and carboxylic acid (–COOH). These results are in line with the EDX spectral data (refer to Section 2.5, Fig. P3, SI). This results in a notable decrease in the C/O

 © 2026 The Author(s). Published by the Royal Society of Chemistry

Open Access Article. Published on 06 January 2026. Downloaded on 3/22/2026 11:27:01 AM.
This article is licensed under a Creative Commons Attribution-NonCommercial 3.0 Unported Licence.

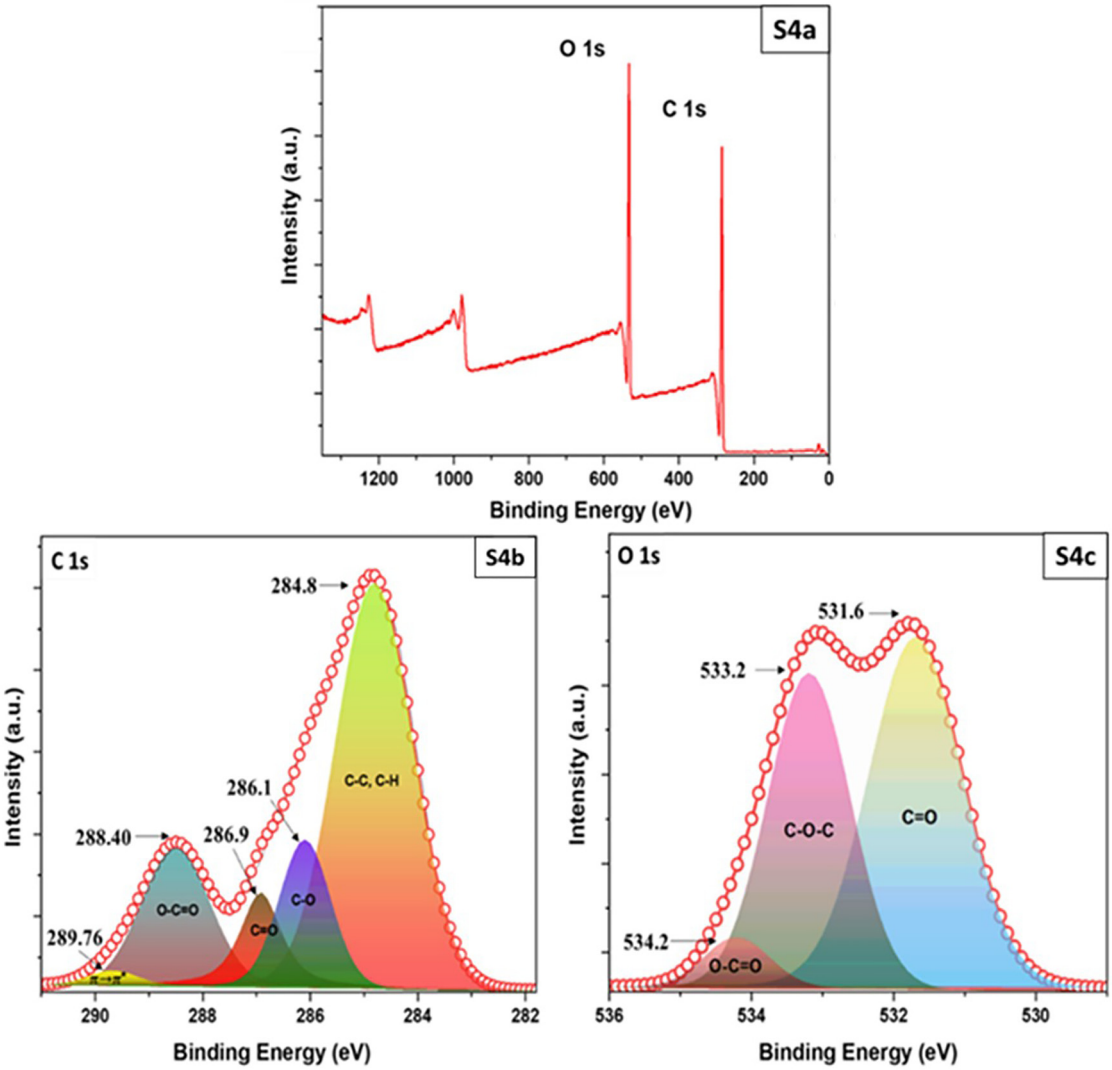

Fig. 6 XPS data for sample S4. S4a: XPS general survey and fitted, S4b: C1s and S4c: O1s peaks corresponding to sample S4. Both C1s and O1s deconvoluted peaks reflect the incorporation of GO into the PMMA matrix. Deconvoluted components C–C, C–O, C═O, and O–C═O, along with $\pi \rightarrow \pi^*$ interactions of C 1s, indicate oxygen-rich functionalities and retention of the graphitic domain.

ratio, clearly indicating an increase in oxygen content due to the oxygen-rich nature of GO.[37] In the high-resolution C 1s spectrum (fitting graph, Fig. 6, S4b), multiple chemically distinct carbon environments are identified through spectral deconvolution. The primary component appears at ∼284.8 eV, attributed to the –C–C- and –C–H bonds originating from the aliphatic backbone of PMMA and the graphitic carbon domains from the basal plane of GO.[38] A second peak around ∼286.1 eV agrees with –C–O– bonds, which can arise from both the ester groups of PMMA and the epoxide/hydroxyl functionalities present on GO sheets.[39] Another component near ∼286.9 eV is associated with –C═O groups, found in the ester linkages of PMMA as well as –C═O or quinone-like structures in GO.[40] A peak at ∼288.40 eV is assigned to O–C═O bonds, such as those in carboxyl/ester groups, and mainly due to both the PMMA's polymer backbone and carboxylic acid moieties present on the edges of GO sheets.[41] The last peak at ∼289.76 is due to $\pi \rightarrow \pi^*$ electronic transitions of GO, due to the retention of the graphitic domain.[42] The increase in the relative intensities of the –C–O, –C═O, and –O–C═O peaks, compared to pure PMMA is a clear indication of successful GO incorporation and the presence of oxygen-rich functionalities.[43]

The high-resolution O1s spectrum (fitting graph, Fig. 6, S4c) further unveils the chemical complexity and surface oxygen content of the nanofibres. This spectrum typically has three dominant contributing peaks and a minor peak, as presented in Fig. 6, S4c. The lower binding energy component, near ∼531.6 eV, corresponds to –C═O bonds, such as those found in ester or –C═O groups. The higher binding energy component, in the range of ∼533.2 eV, arises from –C–O–C– bonds, indicative of the ester of PMMA or epoxide functionalities from GO.[44] In addition, the minor peak at ∼534.2 eV matches –O–C═O due to carboxy moieties present in the edges of GO sheets. The increased intensity and broadening of these peaks,

Open Access Article. Published on 06 January 2026. Downloaded on 3/22/2026 11:27:01 AM.
This article is licensed under a Creative Commons Attribution-NonCommercial 3.0 Unported Licence.

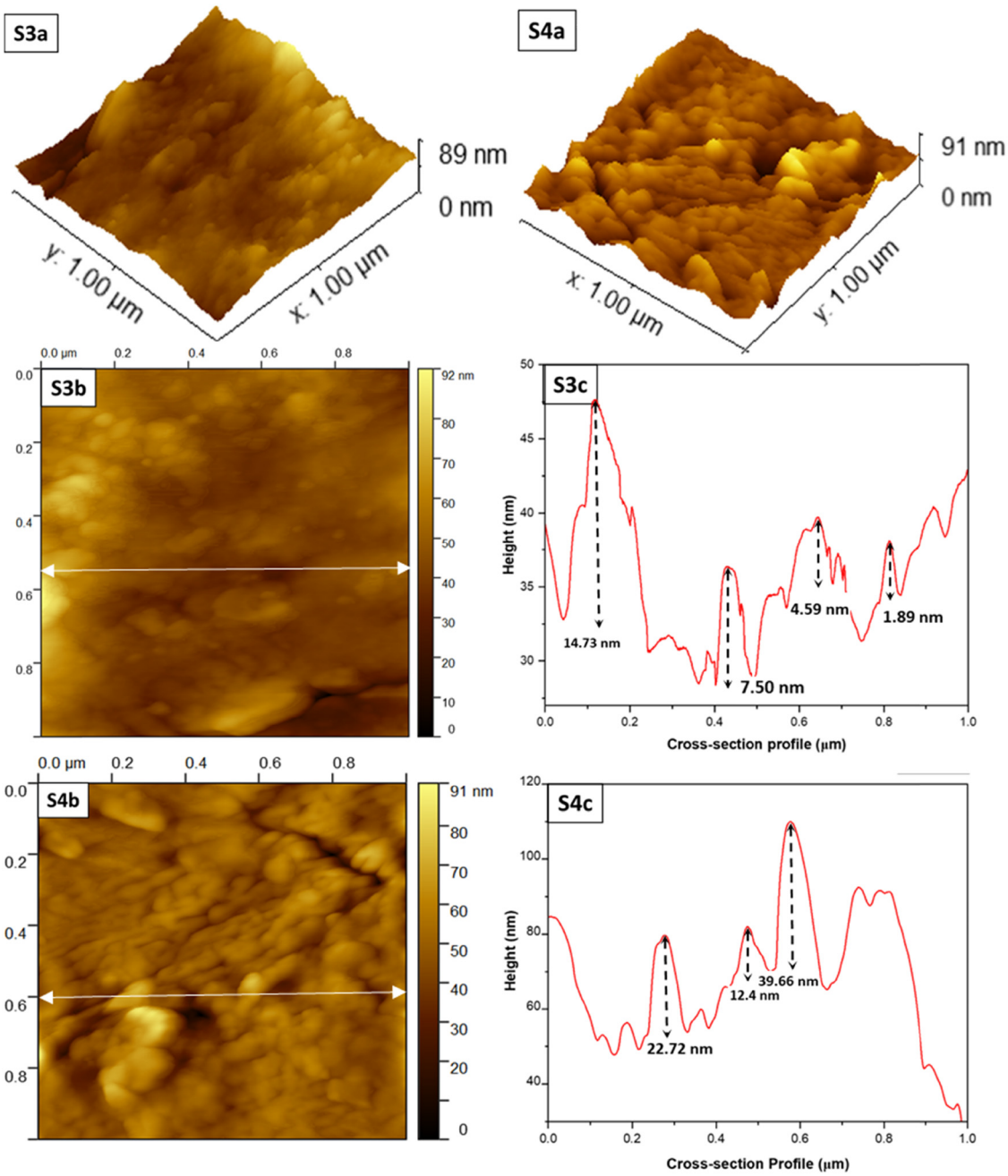

Fig. 7 AFM topography of S3, neat PMMA; S4, PMMA–GO electrospun fibres. S3a and S4a 3D topographical view, S3b and S4b 2D topography, S3c and S4c cross-section profiles for neat PMMA fibres and PMMA–GO fibres. S3 exhibits a relatively smooth and uniform surface with smaller inter-fibre gaps, whereas S4 exhibits a coarser, irregular surface with increased surface roughness.

relative to those observed in pure PMMA nanofibres, reflect the diverse oxygen-containing groups introduced by the GO and their potential interaction with the PMMA matrix. Importantly, the presence and relative proportions of these functional groups also provide evidence for interfacial interactions between PMMA and GO (Fig. 11). The –C═O groups in PMMA particularly participate in H-bonding with –OH/–C═O groups on GO surfaces, and π–π interactions may occur between the GO's conjugated carbon and the PMMA's methacrylate backbone.[45] These interfacial interactions are critical for the improved mechanical and thermal properties observed in the composite nanofibre.

3.3 AFM analysis

3.3.1 Surface topography analysis. AFM data were analysed using *Gwyddion software* (version 2.67), (Fig. 7). AFM topography of neat PMMA appears as an almost uniform and smoother surface, with smaller inter-fibre gaps. This mainly arises from the amorphous nature of electrospun PMMA fibres (Fig. 7, S3a and S3b) and aligns well with the FESEM data. 3D topographical view

 © 2026 The Author(s). Published by the Royal Society of Chemistry

Open Access Article. Published on 06 January 2026. Downloaded on 3/22/2026 11:27:01 AM.
This article is licensed under a Creative Commons Attribution-NonCommercial 3.0 Unported Licence.

of neat PMMA electrospun fibres has a heterogeneous surface with varying heights for S3. The cross-section profile (Fig. 7, S3c), taken along the surface (Fig. 7, S3b), provides a detailed insight into the localised surface roughness. In contrast, AFM images of S4 (Fig. 7, S4a and S4b), also with a cotton-wool-like morphology, typically reveal a highly entangled, fibrous network with pronounced surface irregularities. The topography has considerable height variation across the scanned area, reflecting randomly oriented fibres and their relatively loose packing. The cross-section profile for S4 (Fig. 7, S4c) represents relatively taller surface features, with noticeable increase in peak heights that are likely due to the partial protrusion of GO flakes. This enhanced compactness in the GO-containing fibres is also indicative of improved inter-fibre interactions and possibly better mechanical cohesion.

The most striking observation is the profound change in S4, which depicts a coarser, more irregular surface with a substantial increase in the roughness parameter. Root mean square (RMS) was measured at 21.32 nm and the mean roughness at 16.35 nm. These values represent an ∼2.7-fold increase in RMS roughness compared to neat PMMA fibres, making the surface of PMMA–GO fibres much coarser, with a more irregular surface texture (Fig. 7, S4a). Incorporation of GO has a profound impact by increasing roughness, the presence of larger, more prominent features, which can enhance the effective surface area. The surface topography of PMMA–GO electrospun fibres conveys distinct nanoscale modifications compared to S3. Incorporation of GO generates a more complex surface architecture, evidenced by an increase in RMS roughness (Sq = 21.32 nm from 7.71 nm) as evident from the 3D image view of the surface (Fig. 7S3a and S4a). These changes arise from partially protruding GO nanosheets across the fibre surface. The hybrid surface parameters further convey an ∼8.7% larger true surface area (1.151 μm^2 for S4 *vs.* 1.059 μm^2 for S3). PMMA–GO surfaces show lower skewness and higher kurtosis, suggesting a more homogenous stress distribution under thermal conditions, contradicting localised stress concentrations in neat PMMA. These structural advantages position PMMA–GO fibres as superior candidates for low-temperature applications, especially for cryogenic applications, where nanoscale surface features govern interfacial stress transfer and fracture resistance.

3.3.2 Mechanical property analysis. The mechanical properties of PMMA–GO nanofibres were extensively examined by AFM using peak force quantitative nanomechanical mapping (Fig. 8). The AFM tip indents a specific point on the surface, and it measures the elastic response at that precise location.[11] The overall effective mechanical properties of the mat could appear much more flexible because the measured modulus, reflects the collective behaviour of fibres, their alignment, inter-fibre bonding, porosity, and overall mat density.[11] Thus, AFM-based nanoindentation was employed to investigate the local mechanical properties of a single electrospun fibre.[46] From the topography of height (Fig. 8, S3a, G1), a narrower height distribution (∼1.4 μm) is observed for neat PMMA fibres, whereas for PMMA–GO fibres (Fig. 8ii, S4a, G5), a broader distribution in height (∼2.5 μm) is observed. This indicates that incorporation of GO in S4 has promoted the formation of more independent fibres, whereas for neat PMMA a greater degree of merging of fibres is observed, resulting in uniform morphology.

3.3.3 DMT modulus. The DMT modulus quantifies the stiffness and resistance to deformation of a material.[47] Neat PMMA fibres have a higher DMT modulus, ∼2.04 GPa, while PMMA–GO fibres have a relatively lower DMT modulus, ∼0.28 GPa (Fig. 8, S3b and S4b). The majority of the scanned area appears to be darker in colour for S4, depicting most areas with very low DMT modulus. Even though the present GO loading of 0.39 wt% is sufficient to maintain a stable jet during electrospinning, it is below the critical concentration required to form an effective stress-transfer network within the polymer matrix.[18,48] For a rigid filler to enhance the stiffness, the applied stress must be effectively transferred to the rigid component. At the present GO loading, the nanosheets disrupt the inherent PMMA chain entanglement and packing, which can increase free volume and segmental mobility of the polymer chains.[49–51] This molecular-level interaction can lead to a decrease in the measured DMT modulus. FTIR analysis showed that the interaction between the oxygen functionalities of GO and the –C═O groups of PMMA is dominated by weak non-covalent interactions. The literature on PMMA–graphene-related composites consistently reports that, in the absence of covalent functionalisation, the adhesion energy and interfacial shear strength remain low, leading to inefficient stress transfer and resulting in the nano-sliding effect of polymer chains over the GO surface.[52] This weakly bonded interface thus acts as a plasticiser rather than a reinforcing point, producing a more compliant nanoscale environment and resulting in the reduced DMT modulus. Importantly, this local compliance does not translate to mechanical weakness. Instead, this reflects materials' shift towards increased compliance and flexibility at the nanoscale. The increased compliance facilitates the dissipation of energy and accommodation of contraction under thermal shock, preventing the localised stress buildup.[53,54] This directly contributes to increased flexibility and lowers the apparent modulus at the nanoscale. It is a mode of energy dissipation in polymer systems, which makes it more resistant under cryogenic conditions.

3.3.4 Adhesion. The surface topography of S3 (Fig. 8, S3c, G3) likely shows a smooth surface with uniform adhesion forces, as indicated by a broad distribution histogram, which is possibly due to variations in polymer chain packing. In contrast, S4 has relatively rougher surface topography due to the incorporation of GO. The corresponding histogram exhibits a narrower distribution of counts, indicating variations in adhesion forces across the surface and suggesting that GO may mask the inherent surface adhesion characteristics of PMMA (Fig. 8, S4c, G7).

3.3.5 Deformation. S3 (Fig. 8, S3d, G4) shows very high resistance to deformation (∼12.29 nm), with the majority of the surface darker in colour, which is in line with DMT modulus data for S3. While in S4 (Fig. 8, S4d, G8), most of the scanned area turns out to have brighter (higher deformation) sites. Whereas the resistance to deformation for S4 is ∼15.63 nm. In G4, the deformation values are noticeably more confined to lower values, in comparison to G8, which has values distributed up to ∼100 nm, indicating regions undergoing significantly more

Open Access Article. Published on 06 January 2026. Downloaded on 3/22/2026 11:27:01 AM.
This article is licensed under a Creative Commons Attribution-NonCommercial 3.0 Unported Licence.

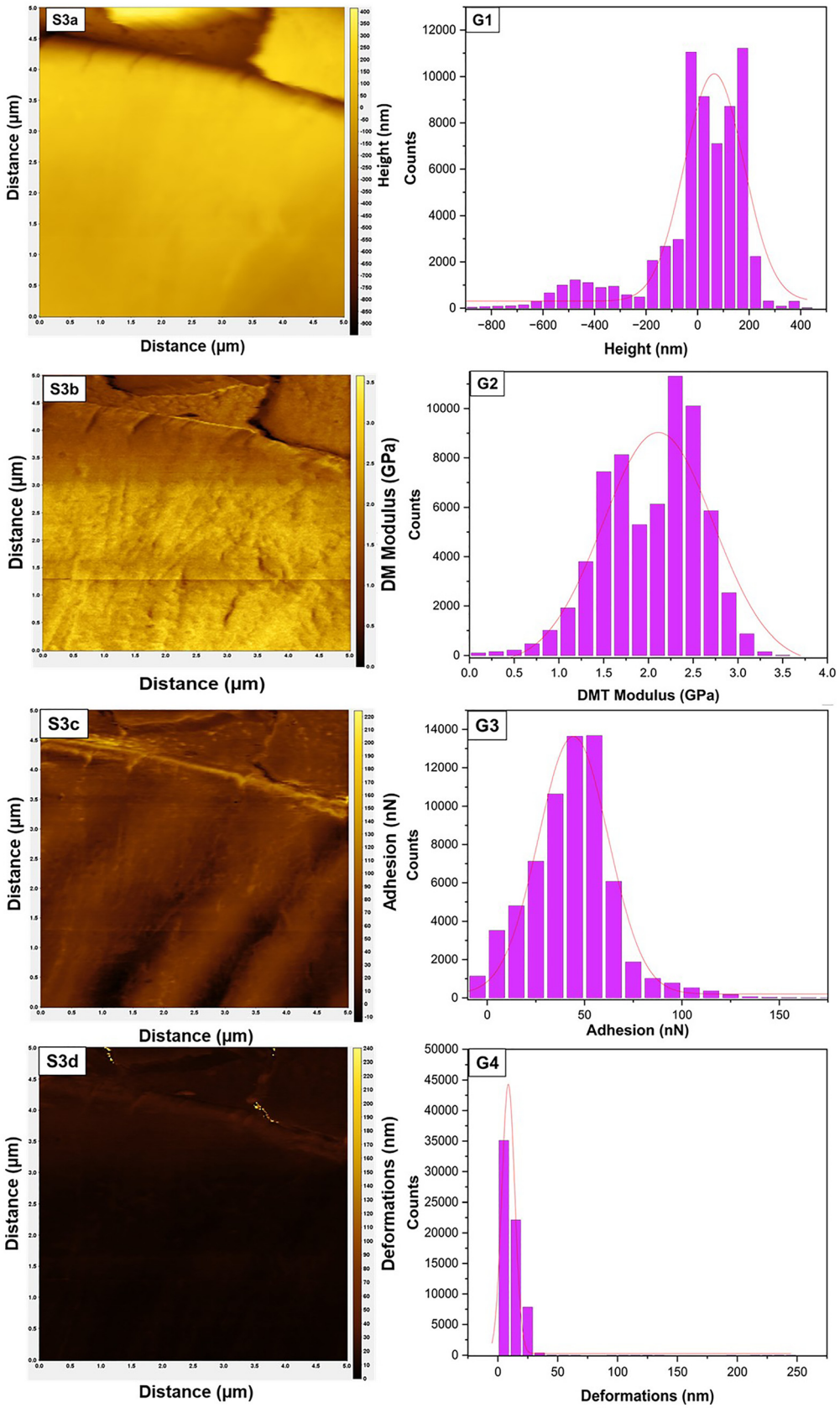

© 2026 The Author(s). Published by the Royal Society of Chemistry

Open Access Article. Published on 06 January 2026. Downloaded on 3/22/2026 11:27:01 AM.
This article is licensed under a Creative Commons Attribution-NonCommercial 3.0 Unported Licence.

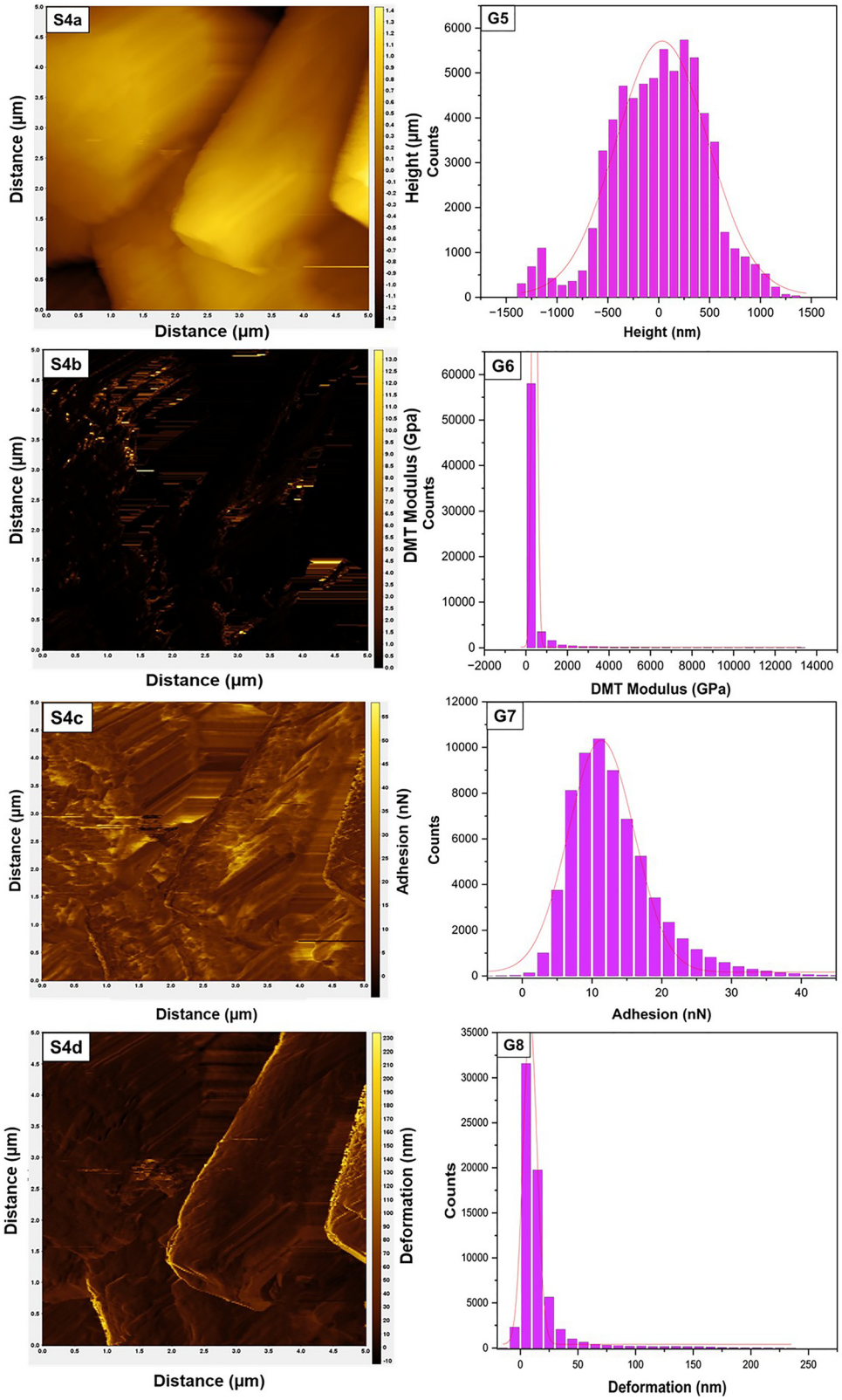

Fig. 8 AFM mapping and distribution of mechanical properties of neat PMMA and PMMA–GO fibres. S3a and S4a: AFM height distribution images, G1 and G5: height distribution histograms, S3b and S4b: DMT modulus maps, G2 and G6: DMT modulus distribution histograms, S3c and S4c: adhesion–force maps, G3 and G7: adhesion distribution histograms, S3d and S4d: the deformation maps, G4 and G8: deformation distribution histograms. It shows that the mechanical response of PMMA fibres after GO incorporation leads to decreased DMT modulus and modified adhesion, indicating enhanced compliance and energy dissipation capability, favorable for resisting stress localisation under cryogenic conditions.

Open Access Article. Published on 06 January 2026. Downloaded on 3/22/2026 11:27:01 AM.
This article is licensed under a Creative Commons Attribution-NonCommercial 3.0 Unported Licence.

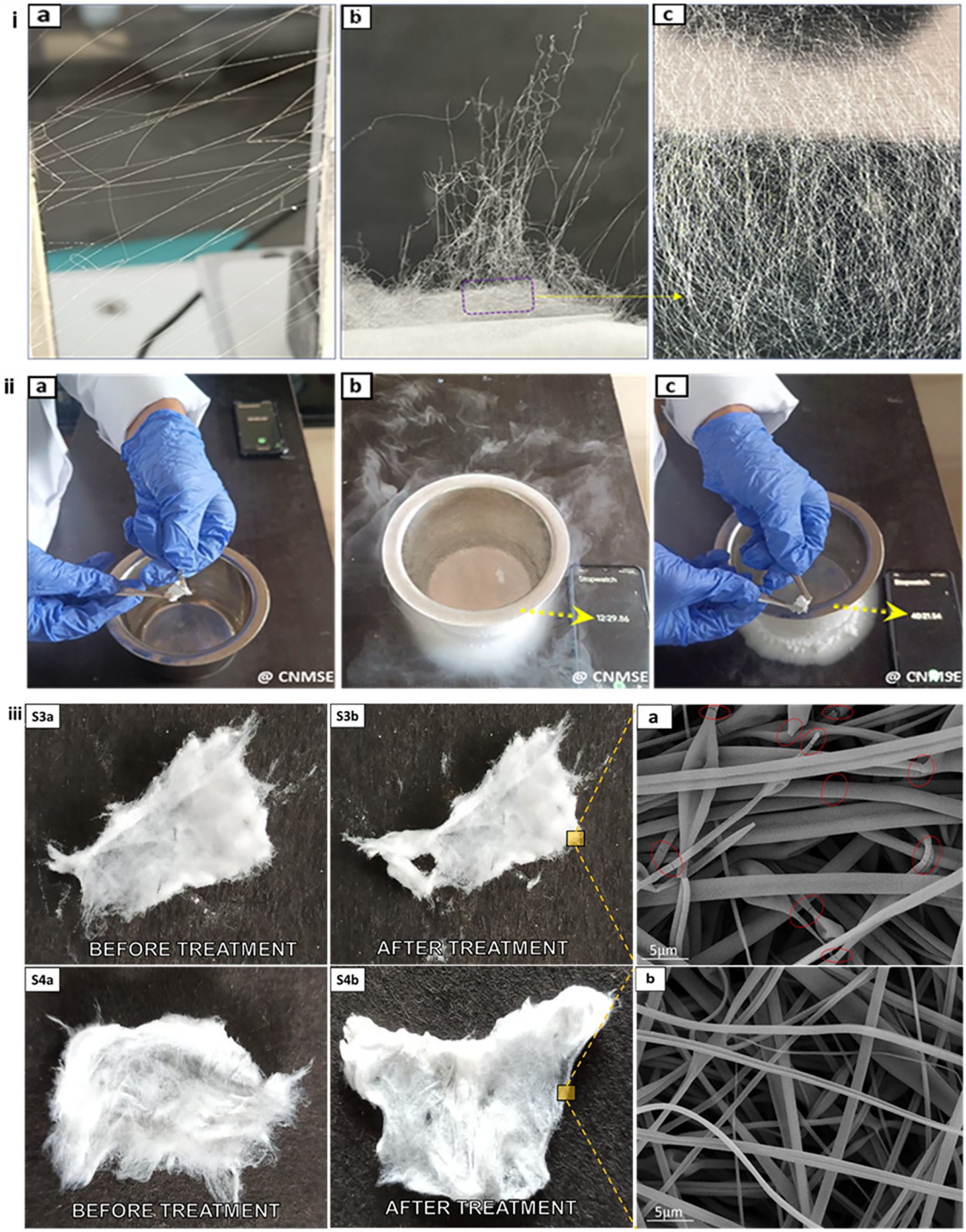

Fig. 9 (i) Digital photographs of GO-reinforced PMMA electrospun fibres depict ultrathin fibres (∼1.5–2.0 μm) with cottony, non-woven architecture. (a) Collected using a metallic grid-frame-like collector. (b and c) Collected in a flat metallic collector covered with aluminium foil. The individual fibres demonstrate exceptional structural integrity, while their porous network arises during electrospinning, resulting in mechanically robust, lightweight nanofibres. (ii) Illustration of liquid N_2 treatment for PMMA–GO electrospun fibres. (a) Testing the flexibility of PMMA–GO fibres before liquid N_2 treatment. (b) PMMA–GO fibres suspended in liquid N_2. (c) Testing the flexibility of PMMA–GO fibres after liquid N_2 treatment for ∼40 minutes. (iii) FESEM data for liquid N_2-treatement: (iii) S3a neat PMMA fibres before and S3b after liquid N_2 treatment, respectively. (a) FESEM image of neat PMMA fibres. S4a: PMMA–GO fibres before liquid N_2 treatment and S4b: PMMA–GO fibres after liquid N_2 treatment, respectively. (b) FESEM image of PMMA–GO fibres. Fibres without the incorporation of GO show the formation of cracks upon cryo-treatment.

 © 2026 The Author(s). Published by the Royal Society of Chemistry

Open Access Article. Published on 06 January 2026. Downloaded on 3/22/2026 11:27:01 AM.
This article is licensed under a Creative Commons Attribution-NonCommercial 3.0 Unported Licence.

deformation than those in S3. A decrease in stiffness doesn't mean a decrease in overall mechanical property; it will be a misinterpretation. Because overall mechanical property encompasses more than stiffness. Despite a lower DMT modulus, it is critical to consider the deformation data. The PMMA–GO fibres still have an extremely sharp peak of 0.2 nm in their deformation histogram, indicating high resistance to localised indentation under the applied force. This suggests that while less stiff overall, the material retains its structural integrity at the nanoscale and does not suffer from excessive plastic deformation upon contact. Therefore, it can be concluded that the incorporation of GO appears to have shifted the mechanical profile of the PMMA fibres towards increased compliance and flexibility.

3.4 Effect of deep cryogenic treatment

To examine the real-world applicability of the developed PMMA cotton-wool-like fibrous system incorporating GO nanosheets (Fig. 9i a–c), its performance, particularly flexibility, brittleness, and behaviour at extremely low temperatures, was systematically inspected. For this purpose, both pure PMMA and PMMA–GO cotton-wool-like fibrous mats were directly immersed in liquid N_2 (Fig. 9ii a–c). Due to the nanoscale and ultrafine nature of the electrospun PMMA fibres, both systems exhibited optimised structural integrity. However, the PMMA–GO system demonstrated markedly superior mechanical stability compared to the pure PMMA nanofibrous specimen. Notably, even after 30 minutes of continuous immersion in liquid N_2, the PMMA–GO electrospun material retained excellent flexibility and elasticity, with no significant increase in brittleness. The macroscopic images (Fig. 9iii and Fig. S3a–S4b) show that both neat PMMA and PMMA–GO fibrous mats retain their overall fibrous appearance after liquid N_2 treatment with little visible deformation. However, the microscopic FESEM images reveal a clear contrast in their structural response. The embedded GO nanosheets form strong interfacial interactions with the PMMA matrix through H-bonding and van der Waals forces, effectively constraining local chain mobility. This improves load transfer and suppresses localised strain accumulation. Furthermore, GO acts as a stress-transfer bridge, enhancing the energy dissipation capability of the fibrous network under thermal shock. This morphology, composed of loosely entangled and randomly oriented ultrafine fibres, allows for deformation accommodation through bending and realignment of fibres rather than fracture, mimicking the mechanics of soft disordered systems.[55,56] At cryogenic temperatures, most polymers experience a glass transition state that limits chain mobility, making them prone to brittleness.[57,58] FESEM confirms negligible structural degradation. Porous architecture lowers thermal conductivity, accommodating

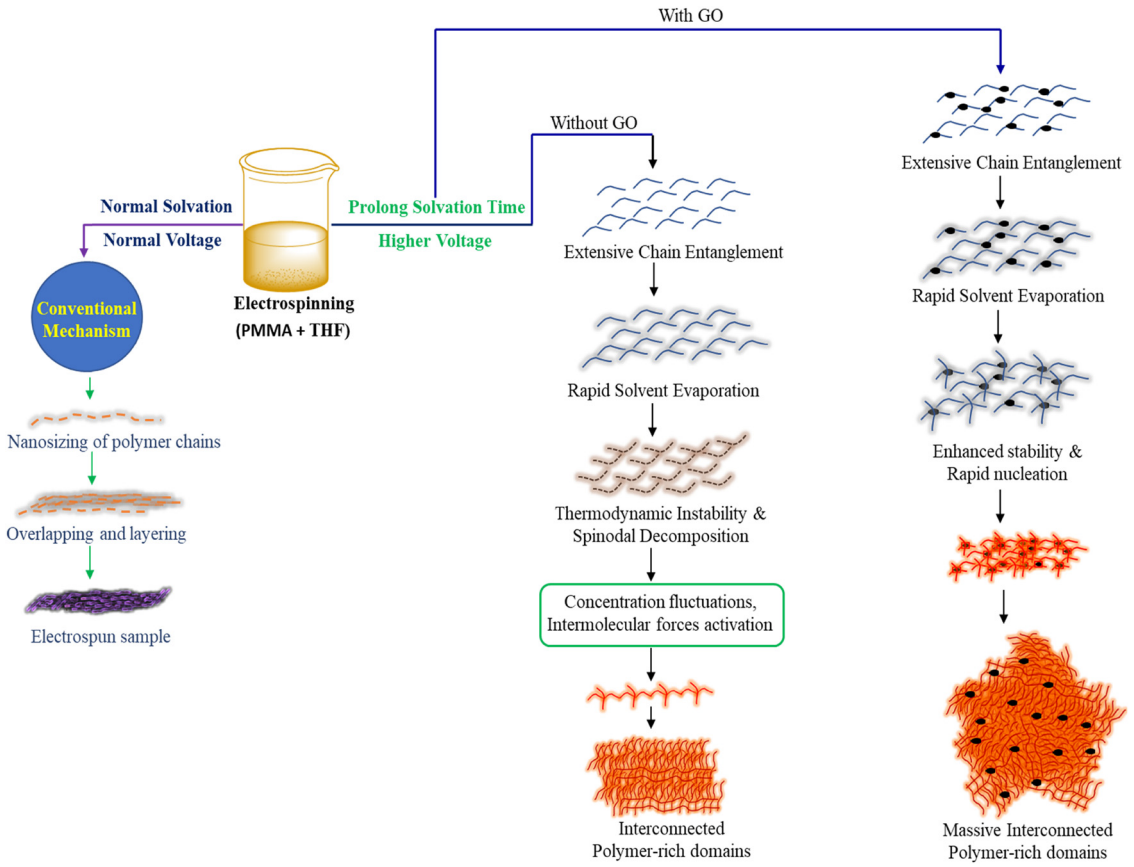

Fig. 10 Schematic representation of the probable mechanism of formation of individually distinct fibres produced *via* an electrospinning technique. The presence of GO can cause extensive chain entanglement, followed by the rapid solvent evaporation during the extensive solvation to produce highly branched, cotton wool-like single fibres.

Open Access Article. Published on 06 January 2026. Downloaded on 3/22/2026 11:27:01 AM.
This article is licensed under a Creative Commons Attribution-NonCommercial 3.0 Unported Licence.

contractions, while GO strengthens the matrix *via* crack deflection and interfacial bonding. It is worth noting that, with only 0.39 wt% GO, the hybrid fibres exhibited exceptional cryogenic stability. The fabricated fibres are not only stable at low temperature, but also exhibit enhanced thermal stability (refer to TGA data in Section 2.6, Fig. P4, SI). The macroscopic images (Fig. 9iii, S3a–S4b) show that both neat PMMA and PMMA–GO fibrous mats retain their overall fibrous appearance after liquid N_2 treatment with little visible deformation. However, the microscopic FESEM images reveal a clear contrast in their structural response.

3.4.1 FESEM analysis of liquid N_2-treated fibres. Investigation of the structure of the fibre by scanning a selectively chosen area revealed that the neat PMMA fibres displayed cracks, upon treating with liquid N_2, whereas GO reinforced PMMA fibres resisted the crack formation and retained the smooth morphology (Fig. 9iii(a and b)). This difference can be due to the reinforcing effect of GO in the PMMA matrix. When exposed to liquid N_2, the polymer fibre underwent plastic deformation caused by thermal shock due to rapid temperature changes. As explained above, GO can bind the PMMA chains together by forming interfacial interactions and help to redistribute stress, thereby delaying the crack growth.

3.5 Probable mechanism of cotton-wool-like fibrous system formation

Based on our experimental work, we concluded (Tiwari hypothesis) that the formation of a cotton-wool-like fibrous system in PMMA is due to the intricate molecular interactions during phase separation and solvent evaporation. At the molecular level, prolonged solvation leads to extensive chain entanglement, forming a metastable network that resists full collapse. As the solvent evaporates, thermodynamic instability drives phase separation, either through spinodal decomposition (in the case of without GO) or rapid nucleation (in the case of with GO). In spinodal cases, continuous concentration fluctuations yield interconnected polymer-rich domains that solidify into fibrous structures, while in the case of GO, the high surface area attributes to massive nucleation. Rapid solidification kinetically traps with disordered morphology, preventing full molecular rearrangement. Intermolecular van der Waals forces and H-bonding stabilise the network, whereas capillary forces during drying induce aggregation of loosely connected fibres. Herein, in electrostatically active PMMA systems, residual charge intensifies repulsion and spatial dispersion, leading to a fluffy texture. The overall morphology arises from a dynamic interplay between polymer–solvent interactions, evaporation rate, and viscoelastic properties, resulting in non-uniform fibrillation and a cotton-like rather than continuously aligned fibrous structure. This morphology reflects a non-equilibrium solidification pathway dominated by intermolecular forces, phase separation dynamics, and chain mobility constraints. Incorporation of GO further amplifies the complexity and mechanical strength. GO nanosheets, with their high aspect ratio and excellent mechanical properties, act as reinforcing

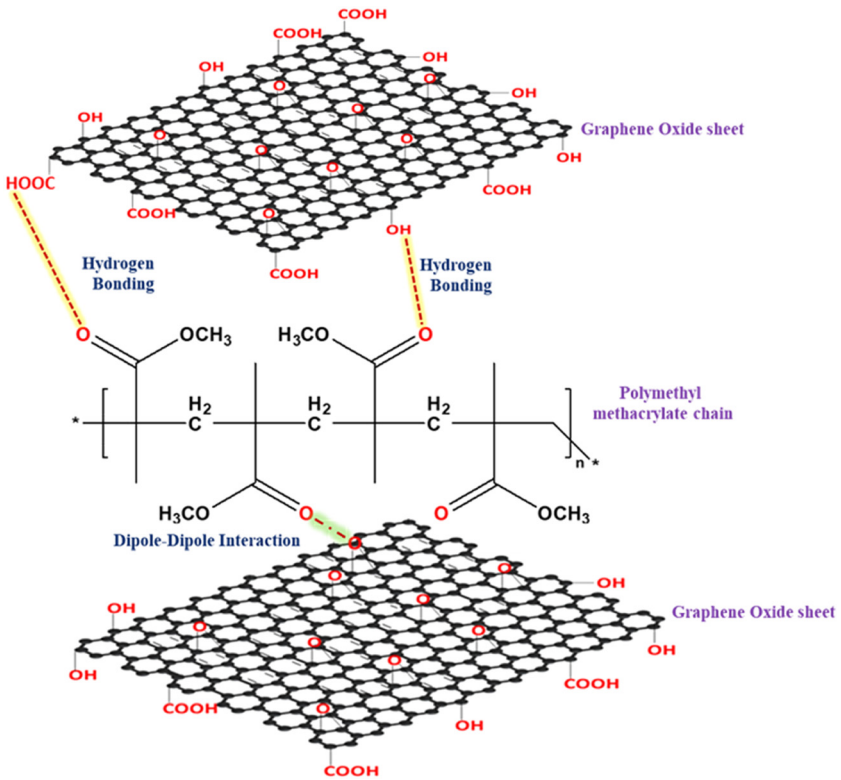

Fig. 11 Probable interfacial interaction based on experimental results between functional moieties present in the PMMA chain and oxygen functionalities present on the GO sheets is demonstrated. It reveals the formation of H-bonding and dipole–dipole interaction, which can potentially strengthen the integrity of PMMA–GO.

 © 2026 The Author(s). Published by the Royal Society of Chemistry

Open Access Article. Published on 06 January 2026. Downloaded on 3/22/2026 11:27:01 AM.
This article is licensed under a Creative Commons Attribution-NonCommercial 3.0 Unported Licence.

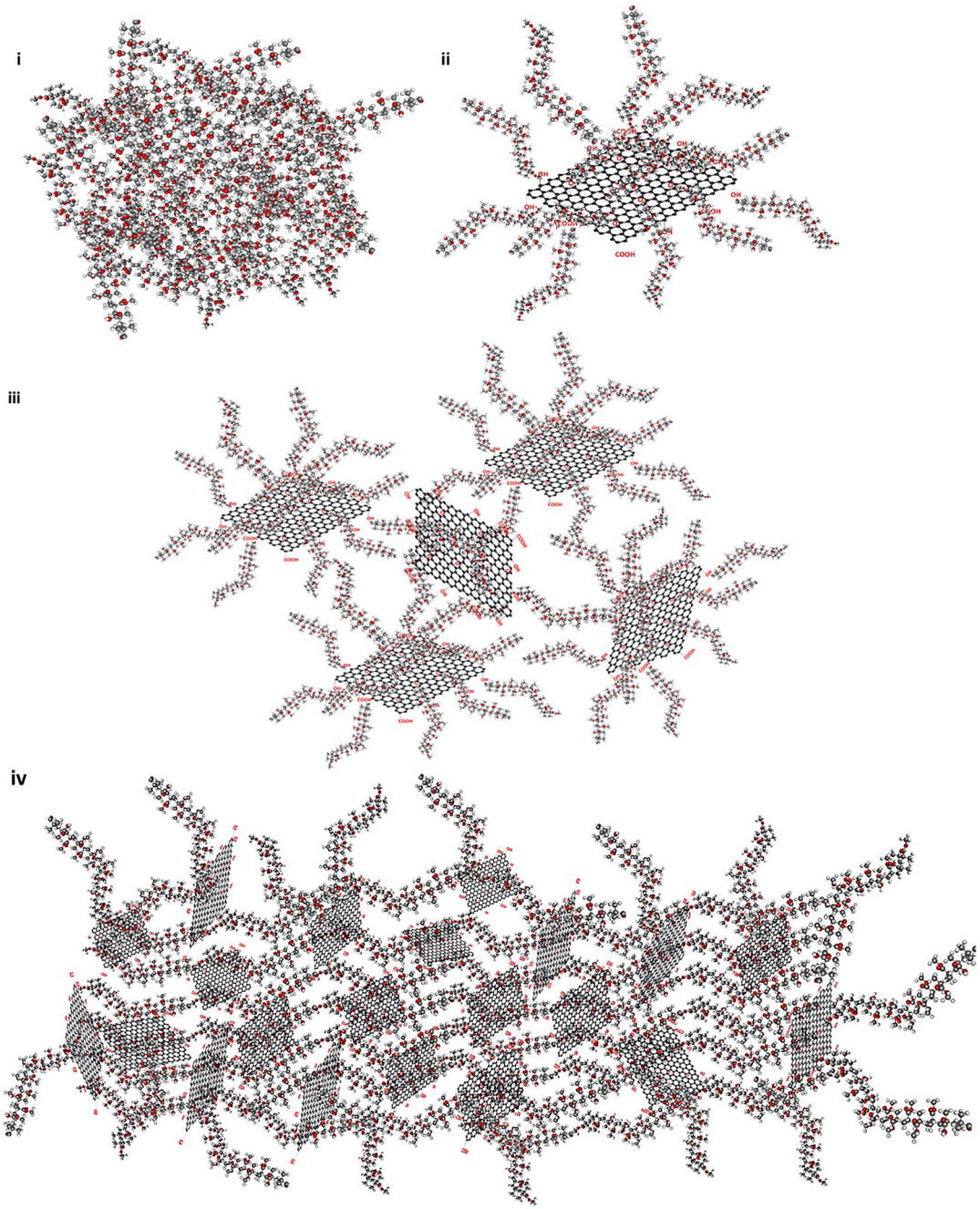

Fig. 12 Schematic illustration of probable molecular orientation of PMMA chains and GO sheets. (i) Randomly oriented and highly entangled PMMA chains. (ii) Initial interactions between the functionalities of GO with the ester moiety of PMMA chains, leading to partial alignment. (iii)–(iv) Progressive alignment and ordered assembly of PMMA chains along the surface of GO sheets, driven by interfacial interactions such as H-bonding and dipole–dipole interactions.

fillers. They serve as heterogeneous nucleation sites during phase separation, promoting the initiation of new fibrous branches and leading to a more intricate, highly branched structure. Crucially, the oxygen-containing functional groups on GO form strong H-bonds and van der Waals interactions with PMMA chains, guaranteeing robust interfacial adhesion. This strong interaction facilitates efficient stress transfer from the polymer matrix to the stronger GO nanosheets, significantly boosting the tensile strength, stiffness, and overall mechanical integrity of the nanofibres. The presence of GO also increases solution viscosity, contributing to kinetic trapping and further stabilising the complex, branched morphology. The probable mechanism is summarised in Fig. 10 and 12. Based on the fundamental physics and physical properties of the polymer chain, we have proposed insight into the formation of distinct fibres and their stability, which is discussed in detail in Section 2.7, SI.

Open Access Article. Published on 06 January 2026. Downloaded on 3/22/2026 11:27:01 AM.
This article is licensed under a Creative Commons Attribution-NonCommercial 3.0 Unported Licence.

3.6 Probable bonding and non-bonding interactions between PMMA and GO

Initially, PMMA chains in solution adopt a random coiled conformation, governed by solvent interactions and entropic effects (Fig. 12i). Upon the introduction of GO, the system undergoes a hierarchical assembly process. The functionalities present on GO act as template sites, driving the ester groups to adsorb onto the GO's surface *via* H-bonding. At the same time, the van der Waals force stabilises the non-polar backbone interactions (Fig. 12ii).[59,60] Over time, thermodynamic equilibrium is approached, as the enthalpic gain from the PMMA–GO interaction outweighs the entropic penalty associated with polymer chain confinement at the GO interface (Fig. 12iii–iv). The net negative free energy change drives the spontaneous adsorption and alignment of PMMA on GO. As the solvent dries, PMMA chains are squeezed closer to GO sheets, further increasing the interfacial adhesion. This alignment reduces chain entanglement in bulk solution, creating regions of asymmetric stress distribution during the final structure (Fig. 12), where GO sheets serve as a 2D scaffold for the PMMA chain. This hypothesis is supported by the spectroscopic evidence, including FTIR peak shifts and XPS data, which validates the increased interfacial interactions between PMMA and GO. The probable sequence of steps involved in the molecular orientation of the PMMA chain on the surface of GO sheets through various interactions is shown in Fig. 11.

4 Conclusion

By systematically optimising the parameters of electrospinning, we were able to fabricate extremely delicate, physically distinct, cotton-like single fibres. It is believed that the synergistic coupling of polymer concentration, viscosity of the solution, and the interfacial interaction of GO with PMMA chains has a significant influence on the formation of individually distinct fibres with unique morphology. Thus, fabricated single fibres were thoroughly studied by employing advanced techniques. Mechanical properties were investigated by employing advanced AFM techniques to precisely focus on a single fibre, to overcome the conventional inconsistencies with the electrospun mat. These findings reveal the enhanced flexibility of GO-reinforced PMMA fibres, owing to the incorporation of GO. Enhancement of thermal stability was verified through TGA, which showed an ∼4.2% increase in decomposition onset temperature. The PMMA–GO fibres were also tested for cell viability, revealing their non-toxic effects on cells in correlation with GO concentration (as mentioned in Section 2.8, SI). The exceptional cryogenic performance of PMMA–GO nanofibres stems from the hierarchical porous microstructure of PMMA–GO fibres, combined with GO reinforcement, which can minimise crack nucleation by redistributing mechanical stresses, thus capable of withstanding cryogenic environments.

Author contributions

ASB: all experimental work, sample preparation, data collection, software, and result optimisation; SJAM: work related to characterisation, data collection, instrumentation; MMD: data collection and experimental support; IA: data collection, referencing, and analysis; GCN: provided pure PMMA and related scientific discussions; JNA: resource, supervision, writing and funding; SKT: conceptualisation, supervision, resource, writing, and funding.

Conflicts of interest

The authors declare no conflict of interest.

Data availability

The data that support the findings of this study are available from the corresponding author upon reasonable request. The supplementary information (SI) contains the methodology for cell viability tests carried out for PMMA-GO reinforced single fibres, along with the characterisation part for GO synthesised, optimisation of GO loading to fabricate the required fibre morphology. Details of spectroscopic (FTIR), thermal (TGA) and elemental analysis (EDS) of PMMA-GO fibres are included. It also discusses the possible physics accounting for the formation of distinct fibres. See DOI: https://doi.org/10.1039/d5ma01000d.

Acknowledgements

SKT sincerely appreciates the support of the MHRD-SPARC project (P3808) under the Indo-UK scheme. Additionally, SKT extends heartfelt gratitude to Nitte University for providing the research grant (Grant no. NUFR-23-070) and MHRD-SPARC (P2527) and ICMR (5/8/5/17/ITRC//2022/ECD-1) for financial support. The author(s) also acknowledge the Central Research Facility (CRF), Indian Institute of Technology Rupar, Rupnagar.

References

1 S. Wu, H. Li and D. N. Futaba, *et al.*, Structural Design and Fabrication of Multifunctional Nanocarbon Materials for Extreme Environmental Applications, *Adv. Mater.*, 2022, **34**, 2201046, DOI: 10.1002/adma.202201046.
2 A. Al-Abduljabbar and I. Farooq, Electrospun Polymer Nanofibers: Processing, Properties, and Applications, *Polymers*, 2023, **15**, 65, DOI: 10.3390/polym15010065.
3 A. Rajput, Upma and S. K. Shukla, *et al.*, Advanced Polymeric Materials for Aerospace Applications, *Aerosp. Polym. Mater.*, 2022, **8**, 117–136.
4 Y. Xu, Q. Saiding and X. Zhou, *et al.*, Electrospun fiber-based immune engineering in regenerative medicine, *Smart Med.*, 2024, **3**(1), e20230034, DOI: 10.1002/smmd.20230034.
5 M. Liu, X. Han and G. Zuo, *et al.*, Soft-hard self-alternating flexible organic-inorganic intercalated short-fiber mimetic bone lamellae, *Composites, Part B*, 2025, **303**, 112581, DOI: 10.1016/j.compositesb.2025.112581.

 © 2026 The Author(s). Published by the Royal Society of Chemistry

Open Access Article. Published on 06 January 2026. Downloaded on 3/22/2026 11:27:01 AM.
This article is licensed under a Creative Commons Attribution-NonCommercial 3.0 Unported Licence.

6 E. Boissin, C. Bois, J. C. Wahl and T. Palin-Luc, Effect of temperature on damage mechanisms and mechanical behaviour of an acrylic-thermoplastic-matrix and glass-fibre-reinforced composite, *J. Compos. Mater.*, 2020, **54**, 4269–4282, DOI: 10.1177/0021998320929056.
7 L. Chang and E. M. Woo, Tacticity effects on glass transition and phase behavior in binary blends of poly(methyl methacrylate)s of three different configurations, *Polym. Chem.*, 2010, **1**, 198–202, DOI: 10.1039/b9py00237e.
8 A. S. Bhat, S. Sahoo and M. M. Devadiga, *et al.*, Polymorphic transformation of seashell waste to develop smart composite films: An environmentally benign and sustainable approach, *Sustainable Chem. Pharm.*, 2025, **47**, 102165, DOI: 10.1016/J.SCP.2025.102165.
9 B. Sun, Y. Z. Long and H. D. Zhang, *et al.*, Advances in three-dimensional nanofibrous macrostructures via electrospinning, *Prog. Polym. Sci.*, 2014, **39**, 862–890, DOI: 10.1016/j.progpolymsci.2013.06.002.
10 H. Zhou, Y. Tang and Z. Wang, *et al.*, Cotton-like micro- and nanoscale poly(lactic acid) nonwoven fibers fabricated by centrifugal melt-spinning for tissue engineering, *RSC Adv.*, 2018, **8**, 5166–5179, DOI: 10.1039/c7ra07453k.
11 T. U. Rashid, R. E. Gorga and W. E. Krause, Mechanical Properties of Electrospun Fibers—A Critical Review, *Adv. Eng. Mater.*, 2021, **23**(9), 2100153, DOI: 10.1002/adem.202100153.
12 B. Ahmad, Synthesis and Characterization of PMMA Nanofibers for Filtration of Drinking Water, *J. Mech. Continua Math. Sci.*, 2019, **14**, 102–116, DOI: 10.26782/jmcms.2019.08.00009.
13 D. P. Ura, J. E. Karbowniczek and P. K. Szewczyk, *et al.*, Cell integration with electrospun PMMA nanofibers, microfibers, ribbons, and films: A microscopy study, *Bioengineering*, 2019, **6**, 1–12, DOI: 10.3390/bioengineering6020041.
14 D. Chen, J. Li and Y. Yuan, *et al.*, A review of the polymer for cryogenic application: Methods, mechanisms and perspectives, *Polymers*, 2021, **13**, 1–29, DOI: 10.3390/polym13030320.
15 K. Selatile, S. S. Ray, V. Ojijo and R. E. Sadiku, Morphological, Thermal, and Mechanical Properties of Electrospun Recycled Poly(ethylene terephthalate)/Graphene Oxide Composite Nanofiber Membranes, *ACS Omega*, 2021, **6**, 21005–21015, DOI: 10.1021/acsomega.1c02578.
16 C. B. Qu, Y. Huang and F. Li, *et al.*, Enhanced cryogenic mechanical properties of carbon fiber reinforced epoxy composites by introducing graphene oxide, *Compos. Commun.*, 2020, **22**, 100480, DOI: 10.1016/j.coco.2020.100480.
17 W. S. Hummers Jr. and R. E. Offeman, Preparation of graphitic oxide, *J. Am. Chem. Soc.*, 1958, **80**(6), 1339–1343, DOI: 10.1021/ja01539a017.
18 D. Li and Y. Xia, Electrospinning of nanofibers: Reinventing the wheel?, *Adv. Mater.*, 2004, **16**(14), 1151–1170, DOI: 10.1002/adma.200400719.
19 S. Li, X. Li and Y. Liu, *et al.*, Interfacial engineering of a plasmonic $Ag/Ag_2CO_3/C_3N_5$ S-scheme heterojunction for high-performance photocatalytic degradation of antibiotics, *Chin. J. Catal.*, 2025, **72**, 130–142, DOI: 10.1016/S1872-2067(25)64652-3.
20 J. Wang, X. Wang and C. Xu, *et al.*, Preparation of graphene/poly(vinyl alcohol) nanocomposites with enhanced mechanical properties and water resistance, *Polym. Int.*, 2011, **60**, 816–822, DOI: 10.1002/pi.3025.
21 L. Singh, A. Kashyap and V. Singh, Investigating the effect of rGO concentration on rGO-PMMA composites synthesized via solution casting technique, *Res. Dev. Mater. Sci.*, 2022, **17**(3), 000912, DOI: 10.31031/RDMS.2022.17.000912.
22 M. A. Kadhim and E. Al-Bermany, New fabricated PMMA-PVA/graphene oxide nanocomposites: Structure, optical properties and application, *J. Compos. Mater.*, 2021, **55**, 2793–2806, DOI: 10.1177/0021998321995912.
23 C. Wang, Y. Wang and T. Hashimoto, Impact of entanglement density on solution electrospinning: A phenomenological model for fiber diameter, *Macromolecules*, 2016, **49**, 7985–7996, DOI: 10.1021/ACS.MACROMOL.6B00519.
24 S. Ramazani and M. Karimi, Aligned poly (ε-caprolactone)/graphene oxide and reduced graphene oxide nanocomposite nanofibers: Morphological, mechanical and structural properties, *Mater. Sci. Eng., C*, 2015, **56**, 325–334, DOI: 10.1016/j.msec.2015.06.045.
25 G. da C. Silva and G. J. M. Fechine, Effect of exfoliation medium on the morphology of multi-layer graphene oxide and its importance for Poly (Ethylene terephthalate) based nanocomposites, *Polym. Test.*, 2020, **90**, 106742, DOI: 10.1016/j.polymertesting.2020.106742.
26 Z. Sekhavat Pour and M. Ghaemy, Polymer grafted graphene oxide: For improved dispersion in epoxy resin and enhancement of mechanical properties of nanocomposite, *Compos. Sci. Technol.*, 2016, **136**, 145–157, DOI: 10.1016/j.compscitech.2016.10.014.
27 C. Wang, Y. Li and G. Ding, *et al.*, Preparation and characterization of graphene oxide/poly (vinyl alcohol) composite nanofibers via electrospinning, *J. Appl. Polym. Sci.*, 2013, **127**, 3026–3032, DOI: 10.1002/APP.37656.
28 B. Wang, Z. Chen and J. Zhang, *et al.*, Fabrication of PVA/graphene oxide/TiO_2 composite nanofibers through electrospinning and interface sol–gel reaction: Effect of graphene oxide on PVA nanofibers and growth of TiO_2, *Colloids Surf., A*, 2014, **457**, 318–325, DOI: 10.1016/j.colsurfa.2014.06.006 Get rights and content.
29 P. Ahuja, S. K. Ujjain, I. Arora and M. Samim, Hierarchically Grown NiO-Decorated Polyaniline-Reduced Graphene Oxide Composite for Ultrafast Sunlight-Driven Photocatalysis, *ACS Omega*, 2018, **3**, 7846–7855, DOI: 10.1021/acsomega.8b00765.
30 S. Ahmad, S. Ahmad and S. A. Agnihotry, Synthesis and characterization of in situ prepared poly (methyl methacrylate) nanocomposites, *Bull. Mater. Sci.*, 2007, **30**, 31–35, DOI: 10.1007/s12034-007-0006-9.
31 W. Pan, H. Zhang and Y. Chen, Electrical and mechanical properties of PMMA/nano-ATO composites, *J. Mater. Sci. Technol.*, 2009, **25**(02), 247–250.
32 S. N. Tripathi, P. Saini, D. Gupta and V. Choudhary, Electrical and mechanical properties of PMMA/reduced graphene oxide nanocomposites prepared via in situ

Open Access Article. Published on 06 January 2026. Downloaded on 3/22/2026 11:27:01 AM.
This article is licensed under a Creative Commons Attribution-NonCommercial 3.0 Unported Licence.

polymerization, *J. Mater. Sci.*, 2013, **48**, 6223–6232, DOI: 10.1007/s10853-013-7420-8.

33 J. Li, J. Guo and H. Dai, Probing dissolved CO_2 (aq) in aqueous solutions for CO_2 electroreduction and storage, *Sci. Adv.*, 2022, **8**(19), eabo0399, DOI: 10.1126/sciadv.abo0399.

34 A. Garcia-Gallastegui, D. Iruretagoyena and V. Gouvea, *et al.*, Graphene oxide as support for layered double hydroxides: Enhancing the CO2 adsorption capacity, *Chem. Mater.*, 2012, **24**, 4531–4539, DOI: 10.1021/cm3018264.

35 S. G. Kazarian, M. F. Vincent and F. V. Bright, *et al.*, Specific intermolecular interaction of carbon dioxide with polymers, *J. Am. Chem. Soc.*, 1996, **118**, 1729–1736, DOI: 10.1021/ja950416q.

36 J. Bürger, V. S. Kunnathully and D. Kool, *et al.*, Characterisation of the PS-PMMA interfaces in microphase separated block copolymer thin films by analytical (S)TEM, *Nanomaterials*, 2020, **10**, 141, DOI: 10.3390/nano10010141.

37 A. Sikora, D. Czylkowski and B. Hrycak, *et al.*, Surface modification of PMMA polymer and its composites with PC61BM fullerene derivative using an atmospheric pressure microwave argon plasma sheet, *Sci. Rep.*, 2021, **11**(1), 9270, DOI: 10.1038/s41598-021-88553-5.

38 A. Kausar, Polymeric nanocomposite via electrospinning: Assessment of morphology, physical properties and applications, *J. Plast. Film Sheeting*, 2021, **37**, 70–92, DOI: 10.1177/8756087920937344.

39 J. Dai and M. Lang, Preparation and mechanical properties of graphene oxide/PMMA and surface-functionalized graphene/PMMA composites, *Acta Chimica Sinica*, 2012, **70**(11), 1237–1244, DOI: 10.6023/A1112231.

40 E. Al-Bermany and B. Chen, Effect of the functional groups of polymers on their adsorption behavior on graphene oxide nanosheets, *Macromol. Chem. Phys.*, 2023, **224**(16), 2300101, DOI: 10.1002/MACP.202300101.

41 E. Paz, Y. Ballesteros and F. Forriol, Graphene and graphene oxide functionalisation with silanes for advanced dispersion and reinforcement of PMMA-based bone cements, *Mater. Sci. Eng. C*, 2019, **104**, 109946, DOI: 10.1016/j.msec.2019.109946.

42 A. Morais, J. P. C. Alves and F. A. S. Lima, *et al.*, Enhanced photovoltaic performance of inverted hybrid bulk-heterojunction solar cells using TiO_2/reduced graphene oxide films as electron transport layers, *J. Photonics Energy*, 2015, **5**, 057408, DOI: 10.1117/1.jpe.5.057408.

43 J. F. Moulder, W. F. Stickle, P. E. Sobol and K. D. Bomben, *Handbook of X-ray photoelectron spectroscopy: a reference book of standard spectra for identification and interpretation of XPS data*, 1992.

44 C. Xu, X. Shi and A. Ji, *et al.*, Fabrication and characteristics of reduced graphene oxide produced with different green reductants, *Plos One*, 2015, **10**(12), e0144842, DOI: 10.1371/JOURNAL.PONE.0144842.

45 S. Wang, H. Chi and L. Chen, *et al.*, Surface Functionalization of Graphene Oxide with Polymer Brushes for Improving Thermal Properties of the Polymer Matrix, *Adv. Polym. Technol.*, 2021, **2021**, 5591420, DOI: 10.1155/2021/5591420.

46 B. R. Neugirg, S. R. Koebley, H. C. Schniepp and A. Fery, AFM-based mechanical characterization of single nanofibres, *Nanoscale*, 2016, **8**, 8414–8426, DOI: 10.1039/c6nr00863a.

47 H. A. Alhadrami, M. Hussain and G. Sewify, *et al.*, Nanofiber Scaffold Coated with Ag and ZnO Nanoparticles for Treatment of Methicillin Resistant Staphylococcus aureus Nanofiber Scaffold Coated with Ag and ZnO Nanoparticles for Treatment of Methicillin Resistant Staphylococcus aureus "Nanofiber Scaffold C", *Am. J. Nanomater.*, 2017, **5**, 24–30, DOI: 10.12691/ajn-5-1-4.

48 K. Nawaz, U. Khan and N. Ul-Haq, *et al.*, Observation of mechanical percolation in functionalized graphene oxide/elastomer composites, *Carbon*, 2012, **50**, 4489–4494, DOI: 10.1016/j.carbon.2012.05.029.

49 X. Han, J. Gao and Z. Chen, *et al.*, Correlation between microstructure and properties of graphene oxide/waterborne polyurethane composites investigated by positron annihilation spectroscopy, *RSC Adv.*, 2020, **10**, 32436–32442, DOI: 10.1039/d0ra05872f.

50 K. I. Choi, T. H. Kim and G. Yuan, *et al.*, Dynamics of entangled polymers confined between graphene oxide sheets as studied by neutron reflectivity, *ACS Macro Lett.*, 2017, **6**, 819–823, DOI: 10.1021/acsmacrolett.7b00416.

51 S. K. Sharma, J. Prakash and P. K. Pujari, Effects of the molecular level dispersion of graphene oxide on the free volume characteristics of poly(vinyl alcohol) and its impact on the thermal and mechanical properties of their nanocomposites, *Phys. Chem. Chem. Phys.*, 2015, **17**, 29201–29209, DOI: 10.1039/c5cp05278e.

52 Y. Chen, Z. Yang, L. Dai and Z. Meng, Impact of graphene oxide arrangement on the mechanical and viscoelastic properties of polymer nanocomposites, *Int. J. Mech. Sci.*, 2025, 297–298, DOI: 10.1016/j.ijmecsci.2025.110351.

53 Z. Li, J. Liu and Z. Zhang, *et al.*, Molecular dynamics simulation of the viscoelasticity of polymer nanocomposites under oscillatory shear: effect of interfacial chemical coupling, *RSC Adv.*, 2018, **8**(15), 8141–8151, DOI: 10.1039/c7ra13415k.

54 Y. Zhao, R. Huang and Z. Wu, *et al.*, Effect of free volume on cryogenic mechanical properties of epoxy resin reinforced by hyperbranched polymers, *Mater. Des.*, 2021, **202**, 109565, DOI: 10.1016/j.matdes.2021.109565.

55 D. Son, S. Cho and J. Nam, *et al.*, X-ray-based spectroscopic techniques for characterization of polymer nanocomposite materials at a molecular level, *Polymers*, 2020, **12**, 1053, DOI: 10.3390/polym12051053.

56 S. Song, C. Wan and Y. Zhang, Non-covalent functionalization of graphene oxide by pyrene-block copolymers for enhancing physical properties of poly(methyl methacrylate, *RSC Adv.*, 2015, **5**, 79947–79955, DOI: 10.1039/c5ra14967c.

57 J. Fan, J. Yang and H. Li, *et al.*, Cryogenic mechanical properties of graphene oxide/epoxy nanocomposites: Influence of graphene oxide with different oxidation degrees, *Polym. Test.*, 2021, 96, DOI: 10.1016/j.polymertesting.2021.107074.

58 I. Serrano-Belmonte, F. J. Cascales-Pérez and V. Pérez-Fernández, Effects of adding graphene fibers to polymethyl methacrylate on

 © 2026 The Author(s). Published by the Royal Society of Chemistry

Open Access Article. Published on 06 January 2026. Downloaded on 3/22/2026 11:27:01 AM.
This article is licensed under a Creative Commons Attribution-NonCommercial 3.0 Unported Licence.

biocompatibility and surface characterization, *J. Prosthet. Dent.*, 2025, **133**(1), 281.e1, DOI: 10.1016/j.prosdent.2024.07.043.

59 M. Sabet and H. Soleimani, Graphene Oxide Impacts the PMMA Characteristics, *Polym. Sci., Ser. A*, 2022, **64**, 860–871, DOI: 10.1134/S0965545X22700535.

60 K. Zarybnicka, F. Ondreas and P. Lepcio, *et al.*, Thermodynamic Parameters Controlling Nanoparticle Spatial Packing in Polymer Solutions, *Macromolecules*, 2020, **53**, 8704–8713, DOI: 10.1021/acs.macromol.0c00698.